Master Thesis

Simulative and experimental investigation of damping strategies for electric motors

Herr cand. aer. Martin Daskalov

April 2026

Nr. 1684

Institut für Luftfahrtantriebe
Universität Stuttgart
Direktor: Prof. Dr.-Ing. S. Staudacher

Institut für Luftfahrtantriebe
Universität Stuttgart
Prof. Dr.-Ing. M. Staudacher

Pfaffenwaldring 6
D-70569 Stuttgart
Telefon (0711) 685 63520
Telefax (0711) 685 63505

Master Thesis

für

Herrn Martin Daskalov Martin Daskalov

Simulative and experimental investigation of damping strategies for electric motors

Hintergrund:

In permanenterregten Synchronmotoren (PMSM) erzeugen elektromagnetisch angeregte Radialschwingungen des Motorgehäuses tonale Geräusche, die durch konventionelle Dämmmaßnahmen nicht reduziert werden können. Für Motoren, bei denen konstruktive Änderungen nicht möglich sind, stellen passive Schwingungstilger den praktikabelsten Lösungsansatz dar.

Wissenschaftliches Ziel/Forschungsfrage:

Entwicklung einer prädiktiven Auslegungsmethodik für ein reibungsbasiertes dynamisches Schwingungstilger-Array zur Reduzierung elektromagnetisch angeregter Gehäuseschwingungen an einem bestehenden PMSM sowie Bewertung seiner Wirksamkeit.

Vorgehensweise

- Literaturrecherche und Klassifikation bestehender Dämpfungskonzepte für Elektromotoren
- Entwicklung und Validierung eines kalibrierten FE-Modells reduzierter Ordnung
- Auslegung, Modellierung und Fertigung eines Reibplatten-Tilger-Arrays
- Nichtlineare Harmonische Analyse zur Vorhersage der Tilgerwirksamkeit
- Experimentelle Validierung durch Motorlauftests

Betreuer:	Tobias Weidemann, M.Sc.
	Lars Weyh, M.Sc. (Deutsches Zentrum für Luft- und Raumfahrt)
Prüfer:	Univ.-Prof. Dr.-Ing. Malte Krack
Verwaltungsbetreuerin:	Heike Fischer

Erklärung des Kandidaten

Ich versichere, dass diese Master Thesis selbständig von mir verfasst wurde – abgesehen von der Mitwirkung der als Betreuer genannten Personen – und dass nur die angegebenen Quellen und Hilfsmittel verwendet wurden.

Ort, Datum

Unterschrift

Termine

Ausgabe:	bestätigt:
Unterbrechung:	genehmigt durch Prüfungsausschuss am:
Verlängerung:	genehmigt durch Prüfungsausschuss am:
Abgabe:	bestätigt:

Erklärung

Hiermit versichere ich, dass ich diese Masterarbeit selbstständig mit Unterstützung der als Betreuer gelisteten Personen angefertigt und keine anderen als die angegebenen Quellen und Hilfsmittel verwendet habe. Die Arbeit oder wesentliche Bestandteile davon sind weder an dieser noch an einer anderen Bildungseinrichtung bereits zur Erlangung eines Abschlusses eingereicht worden. Ich erkläre weiterhin, bei der Erstellung der Arbeit die einschlägigen Bestimmungen zum Urheberschutz fremder Beiträge entsprechend den Regeln guter wissenschaftlicher Praxis[1] eingehalten zu haben. Soweit meine Arbeit fremde Beiträge (z. B. Bilder, Zeichnungen, Textpassagen etc.) enthält, habe ich diese Beiträge als solche gekennzeichnet (Zitat, Quellenangabe) und eventuell erforderlich gewordene Zustimmungen der Urheber zur Nutzung dieser Beiträge in meiner Arbeit eingeholt. Mir ist bekannt, dass ich im Falle einer schuldhaften Verletzung dieser Pflichten die daraus entstehenden Konsequenzen zu tragen habe.

Ort, Datum

Unterschrift

[1] Nachzulesen in den DFG-Empfehlungen zur „Sicherung guter wissenschaftlicher Praxis“bzw. in der Satzung der Universität Stuttgart zur „Sicherung der Integrität wissenschaftlicher Praxis und zum Umgang mit Fehlverhalten in der Wissenschaft“

Contents

Kurzfassung

Die Elektrifizierung des Transportsektors stellt zunehmend höhere Anforderungen an das Schwingungs- und Geräuschverhalten elektrischer Antriebssysteme. In permanenterregten Synchronmotoren erzeugen elektromagnetisch angeregte Radialschwingungen des Motorgehäuses tonale Geräusche bei diskreten Frequenzen, die durch konventionelle akustische Dämmung nicht wirkungsvoll reduziert werden können. Für bereits in Betrieb befindliche Motoren, bei denen konstruktive Änderungen am elektromagnetischen Design nicht möglich sind, stellen passive schwingungsbasierte Dämpfungsmaßnahmen den praktikabelsten Lösungsansatz dar.

Diese Arbeit präsentiert eine vollständige prädiktive Auslegungsmethodik für ein reibungsbasiertes dynamisches Schwingungstilger-Array, das auf die elektromagnetisch angeregte (4,0)-Resonanzmode eines bestehenden PMSM abgestimmt ist. Ein kalibriertes Finite-Elemente-Modell reduzierter Ordnung wurde entwickelt und anhand experimenteller Modaldaten validiert. Die elektromagnetischen Kräfte wurden als harmonische Erregung in die reduzierte Basis projiziert. Ein verstimmtes Blattfeder-Reibplatten-Tilger-Array wurde ausgelegt, modelliert und gefertigt, wobei die nichtlinearen Reibkontakte durch Jenkins-Elemente abgebildet und mittels der Harmonischen Balance-Methode analysiert wurden.

Die nichtlineare Harmonische Analyse zeigte, dass das Tilger-Array unter Teilgleitbedingungen eine Reduktion der maximalen Gehäuseschnelle um bis zu 50% bei der Motorresonanzfrequenz erreicht. Eine Kontaktmechanikanalyse ergab, dass die physische Reibfläche in der gefertigten Ausführung im vollständigen Gleiten betrieben wird, wodurch der für die Tilgerwirkung notwendige Steifigkeitskopplungsmechanismus entfällt. Dies identifiziert die Verifikation des Reibregimes als obligatorischen Schritt in jedem Auslegungsprozess für Reibungstilger.

Das entwickelte Simulationsframework ist validiert, vollständig dokumentiert und direkt auf andere PMSM-Konfigurationen übertragbar und liefert damit eine vollständige prädiktive Auslegungskette für Reibungstilger-Arrays an Elektromotoren.

Schlagwörter: permanenterregter Synchronmotor, dynamischer Schwingungstilger, Reibungsdämpfung, Harmonische Bilanze-Methode, NVH, Modellordnungsreduktion, Jenkins-Element

[2]

[2] Initial draft generated by Claude (Anthropic, 2026), subsequently revised by the author. [4]

Abstract

The electrification of transportation has placed increasing demands on the noise, vibration and harshness behaviour of electric drivetrains. In Permanent Magnet Synchronous Motors, electromagnetically excited radial vibrations of the motor housing produce tonal noise at discrete frequencies that cannot be addressed by conventional acoustic insulation. For motors already in production, where modifications to the electromagnetic design are not feasible, passive response-based damping solutions offer the most practical path to vibration reduction.

This thesis presents a complete predictive design methodology for a friction-based dynamic vibration absorber array targeting the electromagnetically excited (4,0) resonance mode of an existing PMSM. A calibrated reduced-order finite element model of the motor was developed and validated against experimental modal data. Electromagnetic forces were projected into the reduced basis to serve as harmonic excitation. A mistuned leaf-spring friction plate absorber array was designed, modelled and manufactured, with its nonlinear friction interfaces represented by Jenkins elements and analysed using the Harmonic Balance Method.

The nonlinear harmonic analysis demonstrated that under partial slip contact conditions the absorber array achieves up to 50% reduction in peak housing velocity at the motor resonance frequency, with the mistuned split-array configuration providing the best combination of effectiveness and robustness. A contact mechanics analysis revealed that the physical friction interface as manufactured operates in deep gross slip rather than partial slip, eliminating the stiffness coupling mechanism required for DVA effectiveness. This identifies friction regime verification as a mandatory step in any friction DVA design process.

The developed simulation framework is validated, fully documented and directly reusable for other PMSM configurations, contributing a complete predictive design chain for friction DVA arrays on electric motors.

Keywords: permanent magnet synchronous motor, PMSM, dynamic vibration absorber, friction damping, harmonic balance method, NVH, model order reduction, Jenkins element

[3]

[3]Initial draft generated by Claude (Anthropic, 2026), subsequently revised by the author. [4]

1 Motivation

The electrification of transportation is fundamentally reshaping the engineering demands placed on drive systems. Electric motors have moved from niche applications to the central propulsion technology across automotive, commercial, and aerospace sectors, with Permanent Magnet Synchronous Motors emerging as the dominant choice for high-performance applications due to their high power density and efficiency [64], with the NVH behaviour of the electric drivetrain itself moving to the foreground of both passenger perception and product quality assessment.

A well-known source of noise in PMSMs is the electromagnetically excited radial vibration of the motor housing. Radial forces from the interaction between the rotating rotor magnetic field and the stator geometry excite structural resonances of the motor assembly, producing vibrations at discrete frequencies determined by the motor's rotational speed, electromagnetic design, and operating temperature [20] and cannot be attenuated by conventional acoustic insulation, since their frequency and amplitude are tied directly to the operating conditions.

For motors already in production or deployment, where changes to the electromagnetic design or structural architecture are not feasible, response-based vibration mitigation must be applied to the existing structure. Passive dynamic vibration absorbers offer a robust and low-complexity approach. By attaching tuned secondary masses to the motor housing, vibrational energy is transferred from the primary structure and dissipated fully passively, making them particularly attractive for retrofit applications.

Despite the broad literature on dynamic vibration absorbers and electric motor vibrations, no established predictive methodology exists for the design of friction-type DVA arrays targeting specific electromagnetic resonances in existing motor assemblies. In the present thesis a finite element model of a specific PMSM is developed and validated against experimental modal data. A friction plate absorber array is designed, modelled, manufactured, and mounted on the motor. A nonlinear harmonic balance analysis predicts the absorber effectiveness and identifies the optimal tuning parameters. The work contributes a complete and validated predictive simulation chain for friction DVA design on PMSMs, and identifies the contact interface operating regime as critical design parameter.

[1]

[1] Initial draft generated by Claude (Anthropic, 2026), subsequently revised by the author. [4]

2 State of Knowledge

The present chapter covers four interconnected topics, providing the theoretical foundation for the work conducted in the subsequent chapters. The first section introduces Permanent Magnet Synchronous Motors, covering their basic structure, operating principle and vibrational behaviour. The second section describes the electromagnetic force generation mechanism, going over the Maxwell stress tensor and the coupling between electromagnetic excitation and structural mode shapes. The third section provides an overview of existing vibration mitigation approaches for electric motors, from source-based design methods to response-based solutions, with particular focus on dynamic vibration absorber arrays. The fourth section describes the modelling approaches used in the present thesis — structural modelling, electromagnetic force application, Rubin reduction, elastic dry friction elements, and the Harmonic Balance Method.

2.1 Permanent Magnet Synchronous Motors (PMSMs)

Permanent Magnet Synchronous Motors are a class of electric motors in which the rotor magnetic field is generated by permanent magnets rather than electromagnets or induction. This eliminates rotor copper losses and allows for higher power density and efficiency compared to induction motors [64].

The motor structure consists of two principal components — the stator and the rotor, separated by an air gap [59]. The stator comprises a laminated silicon steel core, wound with copper coils in a defined slot pattern. When an alternating current is supplied to the stator windings, a rotating magnetic field is produced in the air gap. The rotor carries permanent magnets arranged around its circumference, which interact with the rotating stator field to produce torque [59]. A section view of a general PMSM can be seen in **Figure 2.1**.

The stator assembly is the primary structural component of the motor. It consists of a laminated silicon steel core pressed into the motor housing, with copper windings wound around the stator teeth and impregnated with epoxy resin [75]. The laminated construction — thin sheets of silicon steel bonded together — is necessary to reduce eddy current losses and results in a composite structure with direction-dependent mechanical properties, discussed in Section 2.4.1. The motor housing encloses the stator assembly and transmits vibrations to the surrounding structure, making it the primary surface of interest for vibration assess-

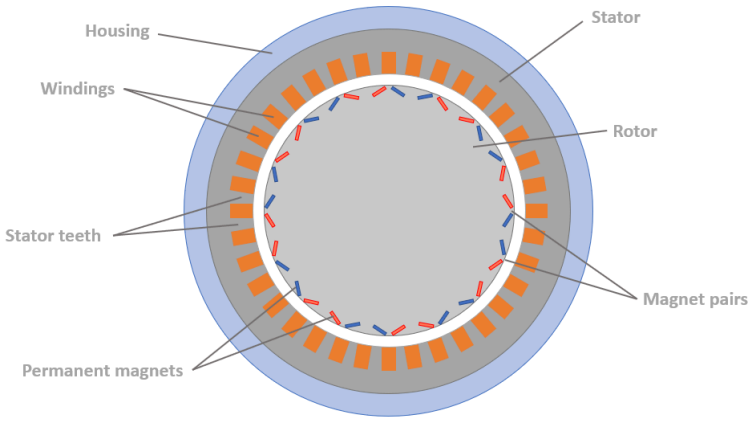

Figure 2.1: Section view of a general Permanent Magnet Synchronous Motor

ment. The rotor is supported by bearings mounted in end shields bolted to both ends of the housing [58].

The motor investigated in the present thesis follows an inner rotor configuration. In it the rotor is positioned inside the stator, which surrounds it. The key geometric parameters relevant to the vibrational behaviour of the motor are the number of stator slots and the number of rotor pole pairs. Together they determine the spatial and temporal order — discussed in detail in Section 2.2 — and define the symmetry properties of the structure. The present motor has 36 stator slots and 16 rotor pole pairs, both with a 4 as the greatest common divisor, giving the motor its quarter cyclic symmetry [13].

2.2 Electromagnetic excitation generation

For electrical machines operating at rated loads the most dominant source of vibrations are those of electromagnetic nature, caused by the magnetic field in the rotor-stator gap [75] [53] [22]. In the present thesis the electromagnetic forces are obtained from an ANSYS Maxwell simulation as described in Section 5.1.7, which captures the dominant harmonics numerically.

The electromagnetic forces arise from the interaction between the rotating magnetic field and the stator field, and act radially on the stator teeth across the air gap, with their spatial and temporal distribution determening the excited structural modes and their frequencies [53], [58], [13]. While axial and tangential components of the forces also get excited during machine operations, their contribution is much smaller than that of the normal components and can be neglected for the purposes of vibration analysis [66] [20] [13] [53][22], especially when the motor mounting stiffness is high [13].

The fundamental mechanism of force generation is described by the Maxwell stress tensor [64] [53], which relates the magnetic flux density in the air gap to the resulting surface force per unit area acting on the stator. As given by [66] its radial component p_r is equal to:

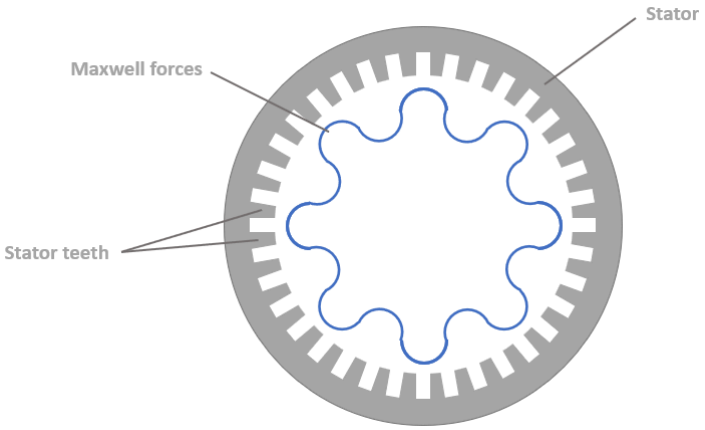

Figure 2.2: Time averaged Maxwell forces acting on stator teeth

$$p_r(\vartheta, t) = \frac{1}{2\mu_0} B_r^2(\vartheta, t) \tag{2.1}$$

where B_r is the radial component of the air gap flux density, μ_0 is the air gap permeability and ϑ is the circumferential position.

The air gap flux density is not uniform around the circumference, but varies periodically due to the stator slot and rotor pole geometry [66]. It can be expressed as a Fourier series in both space and time, with the resulting force density decomposable into spatial and temporal harmonics :

$$p_r(\vartheta, t) = \sum_{\mu} \sum_{\nu} P_{\mu\nu} \cos(\mu\vartheta - \nu\omega_r t - \varphi_{\mu\nu}) \tag{2.2}$$

where μ is the spatial harmonic order, ν is the temporal harmonic order, ω_r is the fundamental angular frequency, and $\varphi_{\mu\nu}$ is the phase angle of each harmonic.

Spatial harmonics describe the variation of the force pattern around the circumference at any given instant — a spatial harmonic of order μ produces a force pattern with μ peaks distributed around the stator. Temporal harmonics describe how the force at a fixed point on the stator varies over time as the rotor rotates. A temporal harmonic of order ν corresponds to a force oscillating at ν times the fundamental electrical frequency. Both exist simultaneously and are linked through the slot and pole pair numbers of the specific motor [75] [64].

In a structure with perfect rotational symmetry, certain structural mode shapes can be oriented at any angle around the circumference and still look identical. These modes are referred to as degenerate mode pairs [60], with the two members having the same natural frequency but with shapes shifted relative to one another. The coupling between spatial harmonic order and structural mode shape is a direct consequence of the orthogonality of mode shapes in cyclic symmetric structures [60]. A force with spatial harmonic order μ can only excite a structural mode with a matching nodal diameter [60], [52]. Thus for a (4,0)

mode with 4 nodal diameters amd 0 axial variations, only spatial harmonics of order $\mu = 4$ contribute to excitation.

The temporal order of the excitation determines at what rotational speed and frequency the resonance condition is reached. For the present motor the critical excitation corresponds to temporal harmonic order $\nu = 32$, which at a rotational speed of 2400 rpm produces an excitation frequency 1280 Hz — coinciding with the (4,0) mode maximum frequency at 35°C motor temperature. The relationship between temporal harmonic order, rotational speed n_{rpm}, and excitation frequency f_{exc} is [60]:

$$f_{\text{exc}} = \frac{\nu \cdot n_{\text{rpm}}}{60} \tag{2.3}$$

The resulting force pattern travels around the stator circumference as a rotating wave, with its wave speed determined by the temporal and spatial harmonic orders. It preferentially excites the forward or backward travelling wave component of the each degenerate mode pair, rather than the standing wave modes observed in free vibration [60]. This travelling wave nature of the excitation is significant for the structural response.

Effects such as the Laplace forces, motor slotting, cogging torque, power supply harmonics and other have also been observed to cause electromagnetic vibrations, but their contribution is generally assumed to be insignificant [52] [20], and were ignored in the present thesis. The Laplace forces are the electromagnetic forces acting on the motor coils, when they are immersed in a dynamic magnetic field [53] [58]. The slotting effects are those caused by the skewing of the motor slots and lead to a non uniform distribution of the magnetic field [66] [53] [58]. Cogging torque represents an unwanted torque generated from the forces of attraction between the permanent magnets in the motor and the motor teeth [13] [53] [58]. Power harmonics are those induced in the motor voltage supply by the puls-width modulator, influencing the electromagnetic forces and increasing their sharpness que to their high frequency [41] [53] [58].

Strong vibrations in electric motors can also have more conventional sources such as bearing wear [52] [13] [53] [22],or rotor-stator eccentricity [13] [22]. Their effects have been ignored during the motor modelling in subsequent chapters, as in the investigated case the electromagnetic excitation is the main vibration source.

2.3 Vibration mitigation approaches for electric motors

A range of approaches exist for reducing electromagnetically excited vibrations in electric motors. They can be broadly classified into source-based methods, which modify the motor itself to reduce the excitation, and response-based methods, which address the structural response to the excitation. Since the motor investigated in the present thesis is an existing design whose architecture cannot be modified, source-based methods are not applicable, but

are briefly reviewed for completeness.

2.3.1 Source-Based Methods

Source-based approaches target the electromagnetic force generation itself, reducing vibration at its origin rather than managing the structural response. They are applied during the motor design phase. The most common strategies include stator slot and rotor pole skewing, optimisation of the slot-pole combination, and modification of the winding configuration

Skewing the stator slots or rotor poles relative to the shaft axis redistributes the magnetic force more evenly along the axial direction, reducing the amplitude of dominant spatial harmonics [27]. Optimisation of the slot-pole combination can shift dominant spatial harmonic orders away from structurally critical modes [75]. Current injection techniques apply corrective harmonic currents through the motor drive and can partially cancel specific force harmonics [33].

2.3.2 Response-Based Methods

Response-based approaches reduce the structural response without modifying its source. They can be subdivided into passive, semi-active, and active methods [56].

Active methods use sensors, actuators, and a control system to apply forces that counteract the structural vibration in real time [56], [48], [30], [76]. Semi-active methods combine passive structural elements with a controllable parameter, typically stiffness or damping, that can be adjusted without supplying energy to the system directly. Magnetorheological [10],[40], [69], [16] and electrorheological [32], [16] dampers for example fall into this category. Passive methods require no external energy input or control system and are therefore inherently robust and simple to implement. Dynamic vibration absorbers are an example of such an approach.

2.3.3 Dynamic Vibration Absorber Arrays

A dynamic vibration absorber (DVA), shown in **Figure 2.3**, consists of a secondary mass m connected through a spring k and damper d element to the primary structure m_0, vibrating under the influence of an external periodic force f. The spring stiffness is used to tune secondary system's natural frequency, with the damping element determening its kinetic energy dissipation mechanism. A classic example is visible in **Figure 2.3**. When tuned to the natural frequency of the primary structure, the DVA absorbs vibrational energy by creating an equal and opposite force to the excitation of the primary strcuture, reducing its response amplitude at resonance [35]. A single DVA achieves its maximum effectiveness when tuned precisely to the target frequency, but its performance degrades rapidly with detuning — making it sensitive to variations in the primary structure's natural frequency [26].

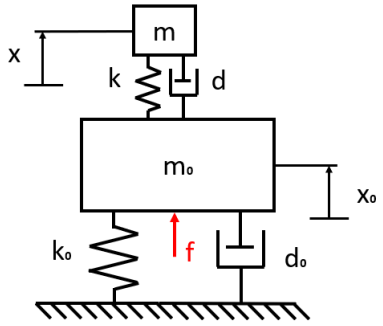

Figure 2.3: Tuned mass damper mounted on a vibrating primary structure

To address this limitation mistuned DVA arrays, consisting of multiple absorbers, tuned to slightly different natural frequencies distributed around the target frequency, have been proposed [26]. By spreading the absorber frequencies across a band, the array achieves a broader effective frequency range than a single optimally tuned absorber, at the cost of a reduced peak attenuation [26]. The natural frequencies of the mistuned arrays for maximising the amplitue reduction at the target frequency can be approximately calculated as:

$$\omega = \omega_0 \pm 0.556\sqrt{\frac{m}{m_0}} \tag{2.4}$$

where ω_0 and ω are the natural frequencies of the primary structure and the absorber, and m_0 and m are their masses. The energy dissipation in the investigated DVA arrays is achieved through elastic dry friction between sliding surfaces. The nonlinear behaviour of such friction interfaces under harmonic loading requires dedicated modelling approaches, described in Section 2.4.4 The physical design of the absorber is discussed in depth in Section 4.3.

2.4 Modeling of electric motors

The simulation of electromagnetically excited vibrations in electric motors requires models that accurately capture both the structural dynamic behaviour of the motor assembly and the nonlinear response of friction interfaces. This section describes the established modelling approaches used in the present thesis — structural finite element modelling, model order reduction, friction interface modelling, and nonlinear frequency response analysis.

2.4.1 Structural Modelling

The structural dynamic behaviour of electric motors is most commonly analysed using the finite element method [11], with their accuracy strongly dependent on model complexity, mesh quality, and the inclusion of appropriate motor subcomponents [22].

The stator is a composite structure consisting of thin silicon steel sheets bonded together

with epoxy resin, whose mechanical properties differ significantly between the axial and radial directions due to the layer interfaces. Similarly the stator windings comprise copper strands impregnated with epoxy resin. Both components are commonly homogenised into equivalent materials with transversally isotropic properties, derived from the volume fractions and properties of the constituent materials using the Voigt and Reuss mixing rules [68], [9]. The accuracy of this homogenisation approach has been validated against experimental modal data in multiple studies and is the accepted standard for electric motor structural modelling [39], [70].

The influence of the motor rotor, especially in inner rotor configurations has a small contribution to the values of the natural frequencies and the mode shape [78]. Its effects on the modal frequencies for simular motors are pronounced mainly in modes with vibration frequencies up to 600 Hz [78], and were assumed to be simular for the current motor. At rotational speeds at about 100 000 min^{-1} and above the motor can exhibit a rotor resonance and high bending forces on the rotor shaft [64], [15].

The end shields contribute meaningfully to the housing stiffness and significantly increase the natural frequencies of the stator modes [68], [24]. They change the load on the stator and thus - the natural frequencies of the modes [75].

For structures with cyclic symmetry the full model can be reduced to a single periodic sector by applying cyclic boundary conditions on the cut faces [60]. This reduces the problem size by a factor equal to the number of sectors with no loss of accuracy, provided the loading and response share the same spatial periodicity. The modal solution for the full structure is recovered by applying phase shifts corresponding to each harmonic index across the sector boundaries. As discussed in Section 2.2, the modes of cyclic symmetric structures are organised into families characterised by their nodal diameter number, and each non-zero nodal diameter mode appears as a degenerate pair [60].

2.4.2 Electromagnetic Modelling

The electromagnetic forces acting on the stator teeth serve as the excitation input to the structural model [58]. The electromagnetic field in the air gap is most accurately computed using two-dimensional finite element analysis, as the magnetic properties of the permanent magnets and stator materials are generally isotropic along the axial direction, making the 2D assumption valid [22]. The radial and tangential force densities acting on each stator tooth surface are obtained from the computed flux density distribution using the Maxwell stress tensor, as described in Section 2.2. The resulting 2D force distribution is commonly assumed to be uniform along the axial direction of the motor and expanded into 3D by replication along the axial coordinate [71]. For practical motor geometries the electromagnetic simulation can exploit the same cyclic symmetry as the structural model, reducing the computational domain to a single sector [14].

The harmonic content of the electromagnetic force is determined by the motor's slot-pole

combination and operating conditions, producing force harmonics at multiples of the fundamental electrical frequency as described in Section 2.2.. The transfer of electromagnetic forces from the electromagnetic mesh to the structural mesh requires a mapping procedure, as the two meshes generally differ in resolution and node positions. Two main approaches are used in the literature. The concentrated equivalent force methods integrate the distributed force over each tooth and apply the resultant at a single node. The nodal force transfer methods maps the distributed force density to the nearest structural nodes based on spatial proximity [58]. The nodal force transfer method preserves more spatial detail of the force distribution and is preferred when the structural mesh is sufficiently refined at the tooth surfaces.

2.4.3 Rubin Reduction

Finite element models of electric motors typically contain a large number of degrees of freedom, making direct use of the full system matrices in nonlinear dynamic analyses computationally prohibitive. Model order reduction techniques condense the system to a much smaller set of generalised coordinates while retaining the essential dynamic behaviour in the frequency range of interest [37].

The Rubin method is one such technique, that constructs a reduction basis from two complementary sets of vectors [37]. The first set consists of the free interface normal modes $\boldsymbol{U}_{\mathrm{K}}$. Those are the mass-normalised eigenvectors obtained from solving the eigenproblem for the unreduced system and capture the global dynamic behaviour of the structure. The second set consists of static constraint modes $\boldsymbol{\Psi}$ and is essentially the responses of the structure to unit displacements at each individual boundary degree of freedom, with all remaining boundary degrees of freedom fixed. These vectors capture the local deformation behaviour at the interface locations, where nonlinear forces are applied.

After computing the two sets, they are made orthogonal to each other to remove all near-linear dependencies and ensure well conditioned reduction basis [21], and are combined to form the transformation matrix T:

$$\boldsymbol{T} = [\boldsymbol{\Psi}, \boldsymbol{U}_{\mathrm{K}}] \tag{2.5}$$

The transformation is then applied to obtain the reduced mass $\boldsymbol{M}^{\mathrm{red}}$ and stiffness $\boldsymbol{K}^{\mathrm{red}}$ matrices, which retain the essential dynamic behaviour of the full system, while greatly reducing the computational requierements.

$$\boldsymbol{M}^{\mathrm{red}} = \boldsymbol{T}^{\mathrm{T}} \boldsymbol{M} \boldsymbol{T} \tag{2.6}$$

$$\boldsymbol{K}^{\mathrm{red}} = \boldsymbol{T}^{\mathrm{T}} \boldsymbol{K} \boldsymbol{T} \tag{2.7}$$

2.4.4 Elastic Dry Friction Elements

The simplest friction model, an idealised Coulomb element, does not accurately capture the finite tangential compliance of physical frictional contact, as it transitions abruptly between a fully stuck and a fully sliding state. Real contacts exhibit tangential deformation before sliding, arising from elastic deformation of the surface asperities at the micro-scale [3].

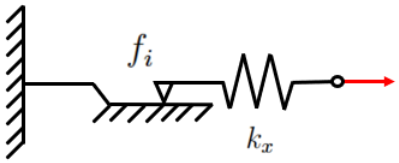

Figure 2.4: Elastic dry friction, or Jenkins, element

A Jenkins elementm shown in **Figure 2.4** addresses this limitation by placing a linear spring with stiffness k_x from the tangential deformation, in series with a Coulomb slip element with a slip force $f_i = \mu_s F_N$, determined by the normal force F_N and the static friction coefficient μ_s [29]. In the stuck state the spring deforms elastically, contributing finite contact stiffness to the system. When the spring force exceeds the maximum static friction force the Coulomb element activates and the interface slides at constant force f_i. Upon load reversal the element returns to a stuck state and the spring begins to deform in the opposite direction, producing a closed hysteretic loop, shown in **Figure 2.5**.

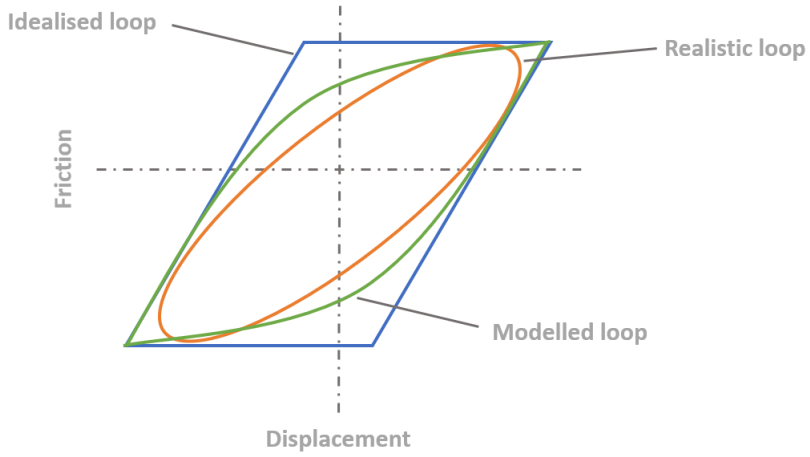

Figure 2.5: Idealised, modelled and realistic hysteretic loop for elastic dry friction

The loading and unloading paths of the hysteresis loop enclose an area proportional to the energy dissipated per cycle. Its rectangular shape is an idealisation, as it does not reproduce the smooth rounded loops observed experimentally for rough surface contacts [46]. A more physically accurate representation is obtained by arranging N Jenkins elements in parallel, each with the same spring stiffness k_x, but with individually distributed slip thresholds. As the applied load increases, individual elements reach their slip thresholds progressively rather

than simultaneously, producing a smooth transition between the fully stuck and fully sliding states. For N elements the generated force [46] can be described by the equation:

$$F = \sum^{N} \frac{f_i}{N} + k_x \frac{N-n}{N} \tag{2.8}$$

where n is the number of elements in a positive yield state. In the partial slip regime, with only a fraction of elements sliding at any instant, the dissipated energy grows nonlinearly with amplitude. Above the gross sliding threshold, where all elements slide simultaneously, it grows linearly. This amplitude dependence is the defining characteristic of friction damping and makes the normal force F_N a physically meaningful tuning parameter. Increasing F_N raises the slip threshold, shifting the onset of gross sliding to higher amplitudes and modifying the effective damping level [46]. The implementation of Jenkins elements for the present friction interfaces and the determination of specific parameter values from rough surface contact models is described in Section 5.1.4..

2.4.5 Harmonic Balance Method

The nonlinear behaviour of friction interfaces under harmonic loading is characterised by hysteretic energy dissipation [46]. Such a system cannot be computed using linear methods, and time-domain methods are computationally expensive for steady-state periodic responses, as they require simulation over many cycles to reach convergence [36]. The Harmonic Balance Method (HBM) provides an efficient alternative by seeking a periodic steady-state solution directly in the frequency domain [36]. The displacement response is assumed to take the form of a truncated Fourier series:

$$\mathbf{q}(t) = \mathbf{Q}_0 + \sum_{k=1}^{H} \left(\mathbf{Q}_{c,k} \cos(k\omega t) + \mathbf{Q}_{s,k} \sin(k\omega t) \right) \tag{2.9}$$

where H is the number of retained harmonics and ω is the fundamental excitation frequency. Substituting it into the equations of motion yields a set of algebraic equations in the harmonic coefficients, which are solved iteratively using a Newton-Raphson scheme [36].

The nonlinear forces at the friction interface are evaluated in the time domain at each Newton-Raphson iteration and transformed back to the frequency domain using an Alternating Frequency-Time scheme [36]. This avoids the need to derive analytical expressions for the nonlinear force harmonics, making the method applicable to arbitrary nonlinear elements including Jenkins friction models. The NLVib toolbox [36] implements this complete framework and is used for all nonlinear frequency response calculations in the present thesis.

3 Purpose of the Present Thesis

The preceding chapter has established the theoretical foundation and the state of knowledge relevant to the present work. This chapter identifies the specific gaps that motivate the thesis, states the research questions that follow from them, and outlines how the subsequent chapters are structured to address them.

[1]

3.1 Identified gaps and Open Problems

The State of Knowledge revealed an established body of work on electric motor NVH modelling and dynamic vibration absorber design. However, the intersection between these two fields: a predictive design of friction-based absorbing strategy targeting specific resonances in existing motor assemblies, has not been systematically addressed in the literature.

Existing NVH studies focus primarily on structural response prediction and source characterisation, with vibration mitigation addressed either through electromagnetic design changes applied during the motor design phase, or through broadband passive treatments. Response-based passive damping using tuned mass absorbers has been demonstrated experimentally for motor stator[18] , but predictive simulation-based design workflows coupling nonlinear friction interface models with reduced-order motor models have not been established.

The nonlinear behaviour of friction interfaces in compact DVA designs for high-frequency electric motor vibration applications — specifically the operating friction regime and its dependence on contact geometry — has not been investigated in this context. Furthermore, as identified in the course of the present work, the sensitivity of the complete DVA design process to the timing and accuracy of electromagnetic excitation frequency data represents an additional open problem.

Thus the present thesis addresses these deficiencies through the following research questions:

1. Which damping concepts are described in the literature for reducing electromagnetically excited vibrations in electric motors, and how can they be classified?
2. How can a tuned friction damper be designed predictively to reduce electromagnetically

[1] Initial draft generated by Claude (Anthropic, 2026), subsequently revised by the author. [4]

excited housing vibrations in an existing electric motor?
3. To what extent is the developed friction damper suitable for reducing housing vibrations?
4. What recommendations can be derived for modelling and tuning?

3.2 Thesis Outline

The research questions are going to be answered across the subsequent chapters. Chapter 2 has already established a systematic classification of damping approaches with particular focus on DVA arrays and friction damping mechanisms. Chapter 4 established the selection and physical design of the friction plate leaf spring absorber array. Chapter 5 developed the validated simulation model. It comprises the reduced-order motor FE model, the simplified absorber model, and the electromagnetic force projection, forming the predictive design basis. Chapter 6 applied the complete framework in a nonlinear harmonic analysis and conducts a parametric study across multiple absorber configurations to determine the optimal absorber tuning. In Chapter 7, the modelling choices and their consequences are critically evaluated, and in Chapter 8, concrete recommendations for future design and tuning are formulated.

4 Dynamic Vibration Absorber Design

This chapter consists of three subsections, which combined cover the complete workflow for the damping concept. The first describes the process behind the selection of a damping concept and energy mitigation method for alleviating the motor vibrations. Objectives are set for bandwidth, amplitude reduction, robustness, energy and control requirements and implementation difficulty. All considered approaches are evaluated and compared, with the most highly rated being chosen for further investigation. The second subsection outlines the design constraints, imposed by the motor geometry and its vibrational behaviour and explains the corresponding design choices for the vibration absorbers design. The third subsection outlines the approach to modelling the complete dynamic absorber and tuning its behaviour in ANSYS Mechanical. This model is the basis on which a simplified dynamic vibration absorber is created and implemented in Section 5.2.

4.1 Damping Method Selection

Multiple literature sources were compared to determine the optimal approach to dampen the radial housing vibration of the investigated electric motor. The method needed to cover vibrations up to 2000 Hz, encountered during motor operation, and a bandwidth or tuning abilities of 200 Hz or more. Additionally it needed to have low power and control requirements, a low mass, affordable cost and be easy to source.

After the general vibration mitigation concept was selected, a second comparison focusing on the implementation of the tuned mass damper array was conducted. Its main objective was to find a simple to implement and easy to tune approach for energy dissipation in the specified frequency band, while avoiding adverse effects like contact between damper and motor surface.

4.1.1 Vibration Reduction Approach Selection

Piezoelectric actuators require a very small measurement error and fast acting control system, and as such are not preffered to mitigate high frequency electromagnetic noise [55], ruling them out for the present application. They were however determined to posses the highest damping effectiveness and precision from the investigated approaches. Experiments have

determined that an increase in displacement speed amplitude of up to 15 dB can be obtained for electric motors [48] with up to 25 dB reduction in sound emissions [6], [76] .

Viscoelastic motor encapsulation was rejected as an approach due to its high weight in comparison to other approaches [55] and reduced effectiveness at frequencies below 2000 Hz [55] - would make them inapplicable for damping the observed electromagnetic vibrations in the specific electric motor at 1100 - 1200 Hz. While it was shown to be a very robust, affordable and easy to install solution [56] for suppressing broadband electric motor vibrations at the 5000 - 10 000 Hz range[58] [43] [56] and is a fully passive approach, its effectiveness is mainly dependent on coverage [43] and layer thickness [58], rather than tunable parameters, making it unsuitable for the current application.

The available experimental results on piezoelectric patche have mainly been in the 150 Hz to 250 Hz range [2] [47], and have shown that the damping forces they apply are fairly small and their effects are highly non-linear, decreasing strongly with increased frequency, and were thus deemed difficult to implement and ineffective for the current application, leading to the choice of a different approach. They were however found to offer the lowest mass contribution to the motor structure, having a weight of up to a couple tens of grams [73] [57]. They also offer impressive theoretical effectiveness at higher frequencies with calculations for piezo patches with negative capacitance shunting suggest they can alleviate vibrations by up to 25 dB over a frequency range of up to 1750 Hz [49].

After reviewing the different approaches, their performance was quantified and scored, with the result in each category being multiplied by a weight coefficient, so that a final ranking can be obtained. The values are available in Appendix Chapter A. It was thus determined that a mistuned distributed dynamic vibration absorber (DVA) array - explained in detail in Section 2.3.3 offered the best balance between performance, ease of integration and availability. It is more robust than a single optimally tuned TMD [26], and offer acceptable performance in the motors operating range [18]. An array has a relatively low mass contribution, can be designed as completely passive, and is easy to source and manufacture [74]. Based on these characteristics the approach was selected for further investigation.

Having chosen a passive mistuned DVA array, a secondary trade-off analysis was conducted to determine the energy dissipation mechanism for the absorbers. Its main objective was to find a simple to implement and easy to tune design for the absorbers, which could then be refined in Section 4.2.

4.1.2 Energy Dissipation Mechanism Selection

Cable vibration absorbers - or also called Stockbridge dampers are mainly intended for damping frequencies between 5 Hz and 50 Hz [67], and could impact the motor housing during operation, due to their large deformation amplitude [7]. Due to these concerns, and the mismatch in the effective frequency, they were rejected as an energy dissipation approach. They were shown however to be the easiest to tune. They consist of two masses attached on

both ends of a steel cable, dissipating energy by the friction between the cable strands [44] and their first eigenvalue could easily be tuned by adjusting the cable or pipe length [34].

On the other hand viscoelastic dampers were determined to be the easiest to implement - due to their wide industry adoption [72], and compact size [77]. As they use the properties of the material for energy dissipation and dynamic stiffness [19], their behaviour is highly nonlinear and temperature dependent, making them difficult to tune [65]. This unpredictable behaviour deemed them unacceptable, and a different method was chosen.

In a similar manner to Section 4.1.1, the performance across different categories was quantified and weighted, with the results shown in Appendix Chapter A. Based on this trade-off analysis the slotted bolted dampers were selected as the energy dissipation mechanism for the dynamic vibration absorbers, since they were shown to offer a good balance between compact design, high effectiveness and easy tunability. They consist of a sliding channel plate sandwiched between outer plates connected with bolts with washers for adjusting the bolt tension and therefore the normal force [17]. They experience small movements during operation and can create strong damping forces [28], but are susceptible to wear and loss of frictional force due to bolt impacts [42], so the bolt pretension needs to be regularly adjusted and restrainers need to be installed to compensate for the effects [42]. These considerations are addressed in the next Section.

4.2 Design Constraints

The vibration absorber design choices were dictated by multiple constraints. Following [74] the absorbers were to be mounted on the locations experiencing the highest vibration amplitudes on the housing. Due to the presence of additional equipment attached on the housing and the motor mounts, the absorber size was limited to a length of 180 mm and a height of 60 mm. This ruled out conventional helical spring designs and led to the choice of a leafspring configuration, due to their slim profile and high stiffness potential. They were to also serve as restrainers to prevent bolt impacts at the end of the friction plate slot, as warned by [42]. They were manufactured out of C45 carbon steel, due to its great balance between its mechanical properties and its abundance in the industry. As compromising the motor housing by drilling in it was unacceptable, the absorbers were designed for adhesive attachment to its outer surface. This was to be done using dual component Loctite EA 9497 epoxy, with its material properties available in Appendix Chapter B.

The absorber normal frequency needed to be easily tunable in the 1060 Hz to 1370 Hz range. This was due to temperature effects on the electric motor, changing its (4,0) mode frequency in the 1225 Hz to 1374 Hz range, while the electromagnetic force frequency at the working point of strongest vibrations, with the motor at room temperature, lay at 1120 Hz. This represents a significant mismatch between the measured modal frequency and the harmonic forcing frequency, and the way it was dealt with is discussed in Section 6.1.3. In order to properly introduce the tuned mass damper array characteristics mentioned in

Section 2.3.3, the damper tuning step size needed to follow the relationships established in [26]. Adjustment of the springs stiffness is the standard approach for tuned mass dampers, with the mass remaining constant. This however proved to be too complex for the current work, due to the need for either replacement springs, or a spring compression mechanism. A mass tuned approach was therefore pursued. This led to the introduction of a 12 weight plate design, which together with the completely unloaded setting provided 13 possible damper configurations covering from 1059.3 to 1374.3 Hz with an average tuning step between them of 22.6 Hz. The modeling procedure which led to obtaining those figures is explained in Section 4.3, with a table showing the relationship between plate count, damper mass and tuned frequency available in in Appendix Chapter D.

As the introduction of additional mass on the motor structure would inadvertently alter its modal characteristics, a weight limit of 2% of the main structure mass was imposed as a project requirement on the damper arrays - a ratio small enough to ensure negligable frequency shift, while in the lower end of what would provide meaningful damping contribution [26]. This led to the adoption of a 6060-T6 aluminium as the material for the middle plate. To give a fine enough adjustment ability to the absorber, the same material was also adapted for the weight plates. For ease of manufacturing, most components were designed to be milled or laser-cut out of standardised L-profiles and plates to produce the desired geometry.

The base and outer plate were initially designed to be manufactured from the same aluminium alloy, but as during the modal simulations it was discovered that their lateral bending mode sits within the motors resonance range at 1318 Hz, reducing the damper effectiveness, they were modified to be manufactured from S235JR + AR 30 mm L-profiles and plates, thus shifting their frequency out of the range of interest to 1800 Hz due to the increased stiffness, leaving the radial movement of the middle plate the predominant mode. A list of the material properties can be found in in Appendix Chapter B.

For predictable sliding dry friction [46], friction zones were established on both sides of the middle plate, and the inner facing side of the base and outer plate, with an arithmetic mean of the absolute values of the profile height deviations from the centre line R_a of the machined surface of 0.8 µm. In order to be able to adjust the plate contact force, and to ensure parallel movement, a slot was added on the middle plate, corresponding to holes on the outer plate and base, with an M4 bolted connection pressing them together. The process for tuning the normal force is explained in Section 6.2.3, when the nonlinear effects are introduced.

In order for the flat bottomed base to be mounted on the convex motor housing, a 0.5 mm deep and 10 mm wide groove was to be machined, thus providing two solid contact edges on both sides of the groove, instead of a single contact point in the middle of the base. The leaf spring thickness and width was chosen within the laser cutter manufacturing tolerances of 0.1 mm to obtain a natural frequency with the lightest absorber configuration as close to the upper desired frequency range boundary. Technical drawings for all of the discussed components can be found in the Appendix Chapter F.

4.3 Complete absorber FEM modelling

The dynamic vibration absorber geometry was modelled and assembled in CAD following the design constraints outlined in Section 4.2 and was imported in its completeness, as seein in **Figure 4.1** in ANSYS Mechanical. The middle and weight plate materials were configured to 6060-T6 aluminium, the outer plate and base to S235JR-AR steel, the leafsprings to C45 steel and the fasteners to generic structural steel, with the material properties available in Appendix Chapter B.

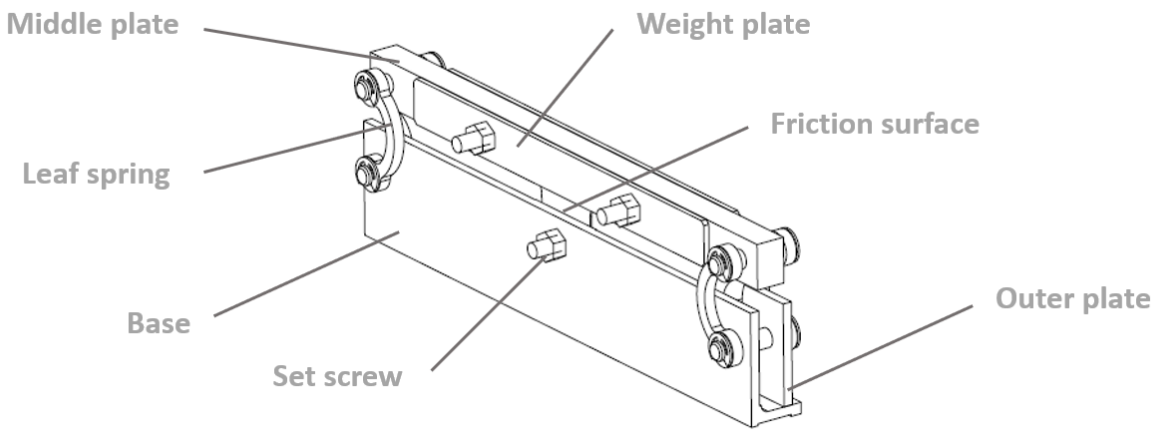

Figure 4.1: Isometric view of the assembled absorber geometry

Several assumptions were made when configuring the contact conditions between the components. Revolute joints were introduced at the attachment points of the leafsprings to the main structure, with the axis of rotation of the joint coinciding with the fastener axis, and the contacts between the leafsprings and the outer plate and base were set to frictionless. The connections between all the fasteners and the corresponding bodies they make contact with were set to bonded, consistent with the intended operational state of the absorber. A slot joint was also introduced at the middle plate slot location, to impose the boundary conditions restricting the middle plates axial movement. The contacts between the middle plate and outer plates and base were set to frictionless to retain all degrees of freedom for the corresponding nodes and enable the subsequent introduction of nonlinear forces.

A fixed support boundary condition was applied to the lower edges of the base, that make contact with the motor outer surface, representing the clamping effect of the adhesive. This is a simplification, as the adhesive stiffness itself is in reality finite, but was deemed appropriate due to the small expected deformations and acting forces. A normal bolt force of 1000 N was applied at the slot connection as a representative preload value, since an acting force is necessary to execute an ANSYS Mechanical structural simulation. Because at the current stage no friction was applied, the normal force does not contribute to the absorber normal frequency, and as such the specific value was inconsequential. To ensure independence of the results from the element size a mesh convergence study was performed for the vibration

absorber model, in a simular manner to the one described in Section 5.1.4 with more details given in Appendix Chapter C. As a result an element size of 1 mm was adopted for the leaf springs, and 5 mm for all other components, as the coarsest size at which all tracked frequencies remained within this threshold.

It should be mentioned that the revolute joint connection introduces a degree of idealisation, since local stiffness contributions are present in the physical assembly, when the leaf springs get clamped between the fastener head and the base surface, that can not be captured by the modelled joint. The assumption was however deemed appropriate as the deformation of the leafspring in the frequency range of interest is bending-dominant, with a negligible axial loading at the attachment points. Additionally, the bonded fastener contacts neglect the deformation of the thread under loading, treating the fastener as a solid beam element. These modelling choices may introduce small deviations between the simulated and physically measured absorber frequencies, which are expected to be partially compensated by the iterative tuning procedure.

An iterative cycle of modal analyses was performed, and the leaf spring geometry was adjusted after each iteration, until the frequency for the first mode of the absorber - the radial movement of the middle plate, was equal to the upper end of the target frequency range at 1370 Hz. After the spring properties have been set, the same iterative design process was repeated for determining the size of the weight plates, ensuring that with a fully loaded absorber the lower end of the target frequency range at 1060 Hz can be reached, with the contribution of the fastener mass also taken into account. At the same time the tuning step size condition established by [26] was maintained. During the initial assembly it was identified that the clearance between the leaf spring attachment fasteners and their corresponding holes in the base and outer plate exceeded the desired tolerance. Replacement components with tighter tolerances were subsequently sourced and fitted, restoring the intended boundary conditions. The full technical drawings of all final absorber components are acessible in Appendix Chapter F.

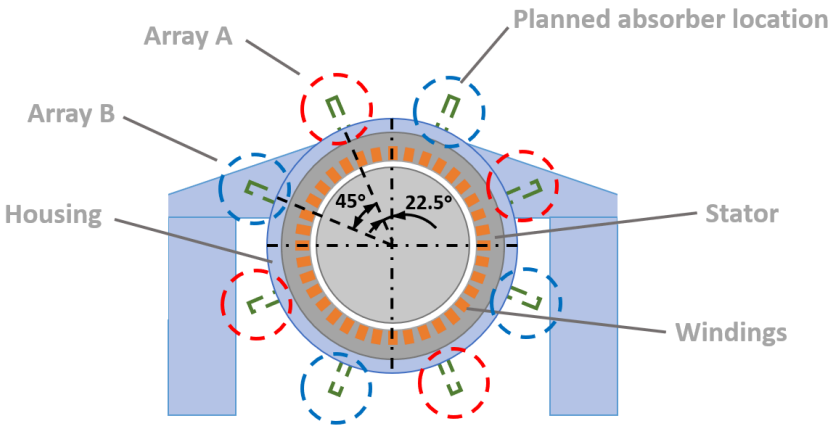

Figure 4.2: Motor with attached absorber arrays

After the absorber design was completed and numerically validated, two absorber arrays were manufactured - each consisting of 4 absorbers, for a total of 8 absorbers. They were to be mounted on the motor as shown in **Figure 4.2**. The finalised absorber design was simplified and integrated into the motor model - discussed more in depth in Section 5.2.1. The normal force and its contribution to plate friction and absorber behaviour are explained in Section 2.4.4 and Section 6.2.3.

5 Simulation Model Development

The current chapter describes the development of the simulation model, used to predict the vibrational behaviour of the PMSM and assess the effectiveness of the dynamic vibration absorber arrays. The model was created with the objective of accurately capturing the motor's dynamic behaviour, while at the same time remaining computationally efficient enough to support the parametric studies in Section 6.2. **Figure 5.1** visualises the steps taken and the software used in building the model and simulating its behaviour.

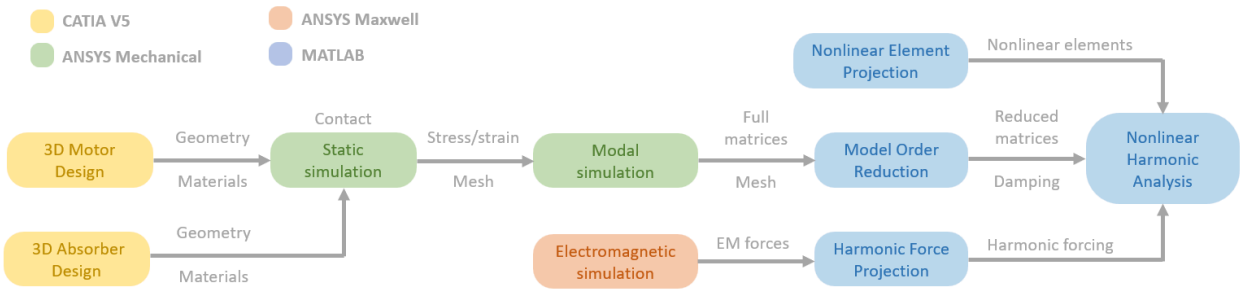

Figure 5.1: Visual representation of the modelling and simulation process

The chapter is divided into two parts. The first section covers the motor structural model — beginning with geometric simplification, going through material modeling, model calibration and order reduction, concluding with electromagnetic force projection to prepare the system for harmonic analysis. The mesh chosen had an element size of 10 mm for the housing, 5 mm for the winding and 10 mm for the stator, based on the findings of a convergence study in Chapter C. The second section describes the simplified dynamic vibration absorber model and focuses on its geometric consolidation and frequency tuning procedure.

5.1 Motor modelling

The steps taken to develop the model can be seen in **Figure 5.1**. First, the geometric complexity of the structure was reduced, by removing the components with negligible contribution. The symmetry of the geometry and electromagnetic forcing was exploited. Finally the composite material properties were represented as equivalent transversal isotropic materials.

A mesh convergence study was conducted on the assembly to determine the element size for each component that ensures result independence. The resulting model was calibrated against experimental modal data and the end-shield influence was introduced. The mass and stiffness matrices of the calibrated model were reduced in order using the Rubin method. The electromagnetic forces obtained from an ANSYS Maxwell simulation were transformed and projected into the reduced basis to serve as harmonic excitation. Each of these steps is described in detail in the following subsections.

5.1.1 Model Simplifications

For the purpose of saving computational resources, while at the same time retaining an acceptable level of accuracy, an important step in creating the simulation model is to omit the components with little contribution to the calculation accuracy and modal evaluation of the motor. The motor support structure is not an original component of the motor assembly, and serves as a solid pedestal for mounting the motor during tests. The coupling between it and the motor assembly however is significant and the boundary conditions they introduce should be taken into account [68]. As such its effects on the modal frequencies and shapes were represented by configuring cylindrical boundary conditions, preventing the axial displacement of the motor housing, and the component itself was removed from the assembly.

As established in Section 2.4.1 the rotor contribution to the modal behaviour of the stator-housing assembly for the current motor falls outside of the rotation range of interest for current motor. The presence of the rotor was therefore omitted.

The rotor and rotor bearings are supported by the end shields, rigidly fastened via 12 bolted connections each to the motor housing in the front and aft part of the motor. After the omission of the rotor their presence in the model is redundant, but their contribution to the housing stiffness is still notable, as discussed in Section 2.4.1. So their influence was introduced by configuring body-to-ground springs - linear bi-directional stiffness elements, for both the front and the aft end. They connected the bolt points on the housing surface with a point coinciding with the center of the front and aft end-shields. The procedure for the tuning of the spring stiffness is explained in Section 5.1.5.

The stator, comprised of the stator yoke and stator teeth has the highest mass and stiffness contribution to the structure [71], and subsequently plays the biggest role in determining the vibration characteristics of electrical machines. The influence of end windings on the stiffness of the model on the other hand is small [39], but their effect on mass distribution within the motor [9] are substantial. Thus they were both retained.

The motor housing was retained due to its major contribution to the vibrational characteristics of the structure [27], but it was significantly simplified, as the number and positioning of the internal cooling channels were not found to be a significant influence on the modal parameters of the motor [9], and were therefore omitted. Following these simplifications the

PMSM was represented by its housing, stator with a yoke and teeth and the full windings with their ends. The final simplified structure is visible in **Figure 5.3**.

5.1.2 Structural Symmetry

To further reduce the complexity the cyclic symmetry of the electric motor was exploited. On one hand the motor itself exhibits quarter geometrical symmetry, being a circular structure with 32 rotor poles and 36 stator slots - with the greatest common divisor being 4. On the other hand the electromagnetic force acting on the stator also acts in a quarter symmetric manner [14]. As a result the (4,0) mode of interest - notation signifying 4 nodal diameters and no axial variations, can be fully represented by a quarter sector model, as spatial harmonics of a certain order only excite natural modes with the same circumferential order [60], [13]. Therefore the motor structure was represented by a single 90° section with cyclic boundary conditions imposed on the section boundaries. The cyclic boundary conditions ensure that motor loading and deformations are rotationally periodic with a phase shift of 90° corresponding to the quarter symmetry.

5.1.3 Material Modeling

The housing is manufactured completely out of an aluminium alloy and has purely isotropic properties. The motor stator on the other hand is composed of multiple laminated silicon steel sheets. The motor winding comprises multiple copper strands, aligned and impregnated together. Therefore they can both be considered composite structures with transversal isotropic material properties, following the theoretical background established in Section 2.4.1.

The composite material density was calculated as the sum of the multiplied densities and volume fractions of the comprising materials [51]. To approximately determine the Young's modulus, Poisson's ratio and the shear modulus, the Voigt and Reuss mixing rules for composite material properties were used [51]. The Voigt rule was applied for the axial properties of the winding and the radial properties of the stator, where parallel stacking was observed, following the approach described in Section 2.4.1. Eq. (5.1) describes its use for calculating the elastic modulus.

$$E_v = \varphi_1 E_1 + \varphi_2 E_2 \tag{5.1}$$

On the other hand for the radial properties of the winding and the axial properties of the stator the Reuss rule was applied, as shown in Eq. (5.2), since the component stacking was in series, resulting in equal stress. The full material properties for all components can be found in Appendix Chapter B. Axis Z coincides with the axial motor direction.

$$\frac{1}{E_r} = \frac{\varphi_1}{E_1} + \frac{\varphi_2}{E_2} \tag{5.2}$$

A notable limitation concerns the modelling of the orientation of the strands in the end windings - using a simple transversal isotropic representation, their directional properties are incorrectly set up, as they are supposed to run tangentially instead of axially. However, since their contribution to the model stiffness is insignificant [39], and their influence on the modal frequencies comes mainly through the extra mass [39], this approach was deemed acceptable.

5.1.4 Contact Modeling

The presence of an interference fit between the stator and the housing, and between the winding and the housing was introduced by configuring the contact to frictional type. The motor was designed with a T7/h8 tolerance at a diameter of 500 mm between the stator and the housing. This leads to an intermediate offset of 0.32 mm for the entire diameter or 0.16mm in radius. A static friction coefficient μ_s of 0.2 was selected. Although a bigger value might have been more accurate for the particular surface contact, ANSYS only allows this value to be set up to 0.2. This was deemed acceptable since increasing the value for the friction coefficient has not been found to have a profound influence, as long as the friction itself is uniformly distributed between each point of the contact face [9]. Since during the manufacturing process the coils are wound around the motor stator and then impregnated with resin, they were assumed to be solidly bonded with it, and as such the contact behaviour in ANSYS Mechanical was set to bonded.

The nonlinear friction contacts of the dynamic vibration absorbers were modelled using Jenkins elements as described in Section 2.4.4. [29], [46]. The two governing parameters — the slip force f_i and the tangential contact stiffness k_T were determined from the specific contact conditions of the absorber friction surfaces.

The slip force f_i is obtained from the equation for static friction and is equal to the normal force applied to the damper via the set screw F_N multiplied by the static friction coefficient μ_s. The friction coefficient for clean aluminium on mild steel friction lies in the 0.61 to 0.7 range [8], [63], depending on surface roughness. The relationship is not linear, and the value in metal on metal friction reaches its minimum close to an average surface roughness of 1 µm [5]. Following the design decisions in Section 4.2., it was assumed that their static dry friction coefficient lies at the lower part of the aforementioned range and a value of 0.61 was chosen.

The tangential contact stiffness k_x was derived from a rough surface contact model following [45], as the sum of the compliance arising from asperity deformation at the rough surface, and an empirical correction equal to the contact stiffness of an equivalent smooth contact geometry.

The nominal contact pressure p at each friction surface over the nominal contact area A_C was computed, with the contact area assumed to cover the entire provided friction surface for every absorber and set equal to 720mm^2.

$$p = \frac{F_N}{A_C} \tag{5.3}$$

From it the surface roughness contribution for the tangential contact stiffness could be computed. It is based on the Greenwood-Williamson framework for elastic rough surface contact. Since the surface distribution for the asperity heights σ could not be measured, a normal distribution was assumed, following [23].

$$k_{t,\text{rough}} = \frac{8G^* p}{E^* \sqrt{\pi \sigma}} \tag{5.4}$$

As the investigated case describes a friction between two different materials - 6060-T6 aluminium and S235AR + JR steel, the composite elastic and shear moduli were used [31], calculated as:

$$\frac{1}{G^*} = \frac{2-\nu_1}{G_1} + \frac{2-\nu_2}{G_2} \qquad \frac{1}{E^*} = \frac{1-\nu_1^2}{E_1} + \frac{1-\nu_2^2}{E_2} \tag{5.5}$$

Finally the combined tangential stiffness, with the stiffness for smooth contact computed using the standard techniques of elastic contact mechanics [31], could be obtained:

$$\frac{1}{k_t} = \frac{1}{k_{t,\text{rough}}} + \frac{1}{k_{t,\text{smooth}}} \tag{5.6}$$

For a normal force of 100N, this value was for example $k_t \approx 4.6 \times 10^7 \text{N/m}$. The nodes on the absorbers friction surfaces were loaded and matched together based on a one millimeter proximity radius, forming 176 node pairs. This proximity radius was chosen to be smaller than the element size used in the mesh generation for the absorber geometry. It should be noted that the pair count depends on the element size for the generated mesh. The calculated friction stiffness and damping parameters were uniformly distributed between the pairs. The corresponding degrees of freedom for each node pair were identified and local elastic dry friction elements with the parameters uniformly distributed between every pair were generated. They were loaded using the nonlinear elements class into the Harmonic Balance solver.

5.1.5 Model Calibration

As described in Section 2.2, each non-zero nodal diameter mode appears as a degenerate pair [60]. In perfectly periodic continuous cyclic symmetric structures they should theoretically be identical [60]. But in a discretised FEM approach the continuous structure is split into multiple elements and during calculation two slightly offset modal frequencies for each mode in the pair are computeted. They converge to a single value as the element size approaches zero [60], but remain present for any practical mesh density. From previous modal hammer tests conducted by the German Aerospace Center it was known that for the specific electric motor the (4,0) free vibration mode at a room temperature of 22°C is encountered at a frequency of 1370 Hz, and at 1280 Hz for a temperature of 35 °C. After running the modal simulation with the previously mentioned boundary conditions and element sizes, the modal frequencies of the (4,0) mode pair land at around 1282 Hz, but still differ by approximately 6% from the test benchmark for room temperature. To calibrate the model the linear stiffness of the springs representing the influence of the end shields on the housing stiffness was varied and the modal frequencies of the (4,0) mode pair were tracked. Following [15], the front and aft end shields were assumed to have equal stiffness contributions, and all spring constants were set to the same value. The model was considered calibrated at the point where the smallest sum of squared errors between the simulated and experimentally measured modal frequencies was achieved. This condition was met at a spring constant of 58500 N/mm, yielding frequencies of 1368.0 Hz and 1372.2 Hz for the two members of the (4,0) mode pair, bracketing the experimentally measured value of 1370 Hz. The relationship between the sum of squared errors and the spring stiffness is shown in Appendix Chapter E.

5.1.6 Model Order Reduction

The sparse mass M and stiffness K matrices for each harmonic index, the nodal coordinates, the DOF map and the IDs of the force and friction nodes were trasnfered to MALTAB. The matrices were assembled into full symmetric shape and scaled to SI units. The Rubin reduction was then conducted as described in Section 2.4.3. The matching nodes on the friction faces of the absorbers were included as boundary degrees of freedom, as these are the locations where the nonlinear elements are subsequently applied. A 3D plot representing them can be seen in blue in **Figure 5.2**. To fully cover the frequency range of interest the first 80 eigenmodes were captured, retaining frequencies up to 7547.26 Hz, equivalent to approximately 3 times the maximum vibration frequency investigated. After reducing the system matrices, the eigenvalue problem was solved for the full $\boldsymbol{M}$ and $\boldsymbol{K}$, and simplified $\boldsymbol{M}^{\text{red}}$ and $\boldsymbol{K}^{\text{red}}$ matrices, and the first 80 eigenfrequencies compared to evaluate the accuracy of the simplification process. The simplification was deemed acceptable and the simplified matrices, together with the transformation matrix $\boldsymbol{T}$ were used in subsequent steps.

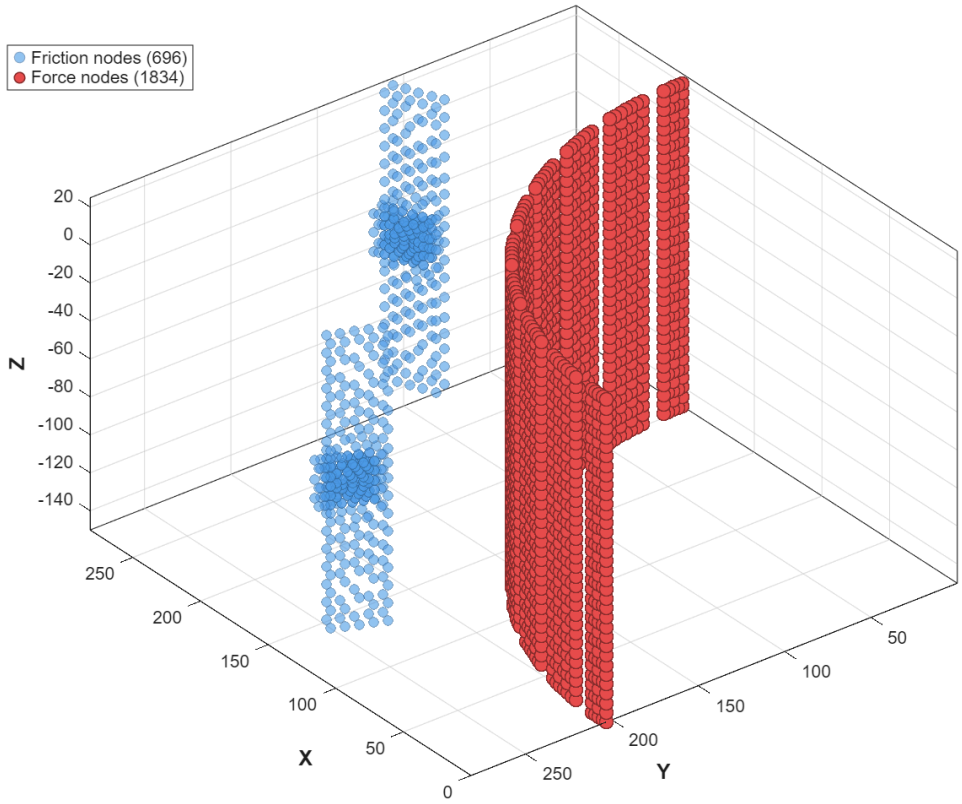

Figure 5.2: 3D spatial distribution of the nodes for force projection

5.1.7 Electromagnetic Forcing

The electromagnetic loading for all work points of interest was obtained from a transient ANSYS Maxwell simulation. The radial symmetry of the motor was also exploited to reduce the computational requirements resulting in 9 teeth per section, with the two teeth on the section boundaries represented by half their geometry, and loaded by only half the electromagnetic force compared to the remaining 7 interior teeth. A sliding mesh was applied in the air gap region to allow relative motion between the rotor and stator during the solve. One full mechanical revolution was simulated at no-load. The Maxwell equations Eq. (2.1) were solved in 2D for the radial B_r and tangential B_t air gap flux density, the force density vectors $p(\vartheta, t)$ were integrated over the tooth width, and scaled by the axial lenth of the machine to obtain the equivalent 3D forces. This was done under the assumption for an ideal motor comprised completely of isotropic homogenous materials, ignoring the effects of manufacturing inconsistencies. The vector potential outside the defined region, bigger that the stator outer diameter, was assumed to be zero. The forces and moments in each cardinal direction for every harmonic were exported in complex form, together with information about the coordinates and direction for each stator tooth.

The provided loading harmonics were filtered to the range of interest between 100 Hz and 2500 Hz. The harmonics with a peak force magnitude across all teeth under one Newton were discarded, as their contribution is insignificant in comparison to the 50 N to 400 N observed force magnitude of more dominant harmonics. The lowest base frequency was identified and

the number of retained harmonics was recorded for each work point. The loads for each tooth were then matched to the corresponding nodes based on their proximity in the radial coordinates within a matching radius of 12 mm, corresponding to slightly more than half the tooth width. They were then uniformly distributed between said nodes, with the 3D spatial distribution visible in red in **Figure 5.2**. The complex physical force vectors were then distributed to the corresponding degrees of freedom and projected into reduced basis from the Rubin reduction [37] following the formula:

$$\hat{\boldsymbol{f}}' = \boldsymbol{T}^{\mathrm{T}} \hat{\boldsymbol{f}} \tag{5.7}$$

where $\hat{\boldsymbol{f}}'$ is the projected force vector and $\hat{\boldsymbol{f}}$ is the physical force vector.

This was done separately for the base frequency and for the complete force excitation matrix to get them in the required format as NLVib requires the base frequency and force harmonics as separate inputs [36] for further use in the harmonic analysis in Chapter 6.

5.2 Simplified absorber FEM modelling

The simplified simulation model of the dynamic vibration absorber was derived from the complete CAD geometry developed in Section 4.3, following a similar modelling philosophy to Section 5.1. The following subsections describe the process in detail.

5.2.1 Model Simplifications

Since the base and the outer plate only act as a stationary mounting solution and friction surfaces, and do not contribute to damper effectiveness in any other way, they were combined into a single solid component with a simplified geometry. Their initial length, width and height were retained, but fastener holes were removed and the mounting groove on the lower base surface was replaced with a concave surface, matching the curvature of the motor outer housing. The weight plates and fasteners were integrated into the middle plate geometry, with their mass effect instead captured through adjusting the simplified middle plate density. On the middle plate, fastener holes and curved edges were again removed, and the sliding slot was simplified to a rectangular cutout with an identical size. The effects of the leaf springs were represented by four linear bi-directional spring elements, connecting the edges of the simplified base with the edges of the simplified middle plate at each of the four corners. The procedure for tuning their stiffness across the entire operational frequency range is explained in more detail in Section 5.2.2.

The material properties for the simplified base were identical to those for the initial absorber design in Section 4.3 for S235JR + AR steel. For the middle plate a 6060-T6 aluminium alloy was configured, and the material density was adjusted to account for mass contribution of

the integrated fasteners. The contact between the simplified base and the motor housing was set to bonded, representing a solid mounting solution. Frictionless support boundary conditions were added on the slot sides facing the front and the back to prevent unrealistic axial movement due to the lack of fasteners in the model. This condiiton is practically realised by the presence of a fastener in the slot in the physical absorber.

The bodies were meshed with second order tetrahedral elements and contact matching was configured on the friction faces of both the simplified base and simplified middle plate. This mesh modification guarantees that overlapping nodes were created as node pairs for both bodies, to which nonlinear elements could be later introduced. A small mesh convergence study to find the element size leading to independent results was conducted. As the obtained values were shown to be effectively independent of element size the largest element size permitting proper mesh generation with contact matching of 20mm was selected.

The final simplified absorbers were attached in an array configuration on the simplified motor section. They were positioned axially in the middle of the housing, with their central plane facing radially to the motor center. This finalised model visible in **Figure 5.3**

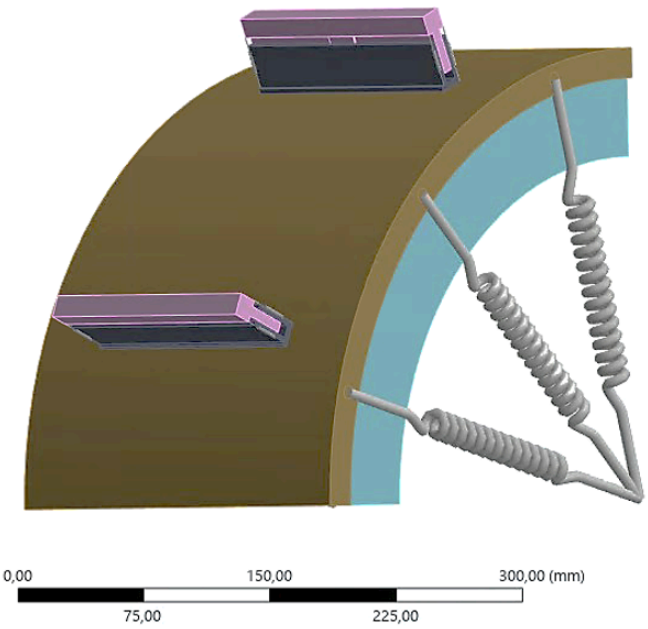

Figure 5.3: Simplified motor section with an attached absorber array

5.2.2 Frequency Tuning

The total weight of the moving components of the full absorber - middle plate, weight plates and fasteners was calculated for all different frequency configurations and adjusted simplified middle plate densities were calculated for each one of them. The resulting densities and tuned frequencies can be found in Chapter D.

To calibrate the simplified model and obtain a behaviour consistent with the full dynamic vibration absorbers, the linear springs were tuned. The goal was to identify the spring stiffness value that produced the same modal behaviour as the full dynamic vibration absorber model across all weight configurations. Three absorber settings were chosen - a low-frequency setting (12 weight plates), a mid-frequency setting (6 plates), and a high-frequency setting with purely the weight of the middle plate. The frequencies of the target mode, were therefore 1374.3 Hz, 1177.8 Hz and 1059.3 Hz. The linear spring stiffness was then varied in unison until the smallest sum of squared errors between the simulated modal frequencies for the full and simplified absorber was achieved. This condition was met at a spring constant of 2435 N/mm, yielding frequencies of 1391,8 Hz, 1171.70 Hz, and 1051.1 Hz accordingly with an average error of 0.85%

6 Nonlinear Harmonic Analysis

In the current chapter nonlinear harmonic analysis was performed to assess the vibrational behaviour of the motor and evaluate the effectiveness of the dynamic vibration absorber arrays. It is split into two parts. The first part establishes a validated baseline frequency response of the motor without absorbers. In the second part the nonlinear friction elements representing the absorber arrays are introduced and the optimal damper setting in terms of vibration amplitude reduction was determined.

6.1 Baseline frequency response

Before the absorber effectiveness could be assessed, a validated baseline of the motor's behaviour was required. A baseline was established through a combination of experimental measurements and simulation.

Firstly, modal hammer tests were conducted across a range of motor temperatures to determine the temperature-dependent frequency of the investigated mode and identify a suitable resonance operating point. Motor running tests were then performed to quantify the vibration amplitude at the measurement points under operating conditions. Finally, a linear harmonic analysis was performed and calibrated against the experimental results through Rayleigh damping, ensuring that the simulation reproduces the measured motor behaviour with acceptable accuracy.

6.1.1 Experimental Modal Analysis

To determine modal frequency of the motor, repeated modal hammer tests were conducted. An automatic modal hammer was positioned so that each strike vector was pointed towards the motors center. It comprised a modal hammer with force measurement capabilities, a controllable stepper motor, and power and control units. One strike per measurement point was performed with a strike velocity of 200°/sec with a time interval between each strike of 5500 ms and a stop angle of 0.3° past contact ensuring a single clean impact. This resulted in a strike force of between 510 N to 515 N. 53 measurement points were established on the motor outer surface - a 9 by 6 grid, forming a sector of approximately 22.5°. One point was laying too close to the motor cooling pipe and was thus excluded from the measurement.

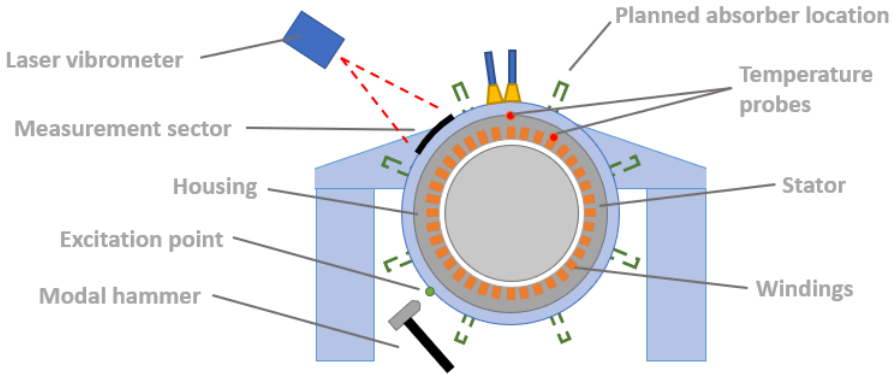

Figure 6.1: Experimental modal analysis setup

The deformation and mode shape was measured with a single axis laser vibrometer. The measurement was performed at room temperature (assumed to be 22°C) and repeated for 30°C, 35°C, 40°C, 50°C, 60°C and 70°C stator temperature, as determined by two Regloplas Pt100 thermo couples mounted as shown in **Figure 6.1**. The motor temperature was increased after every measurement by spinning it up until the desired condition was reached as detected by both temperature sensors.

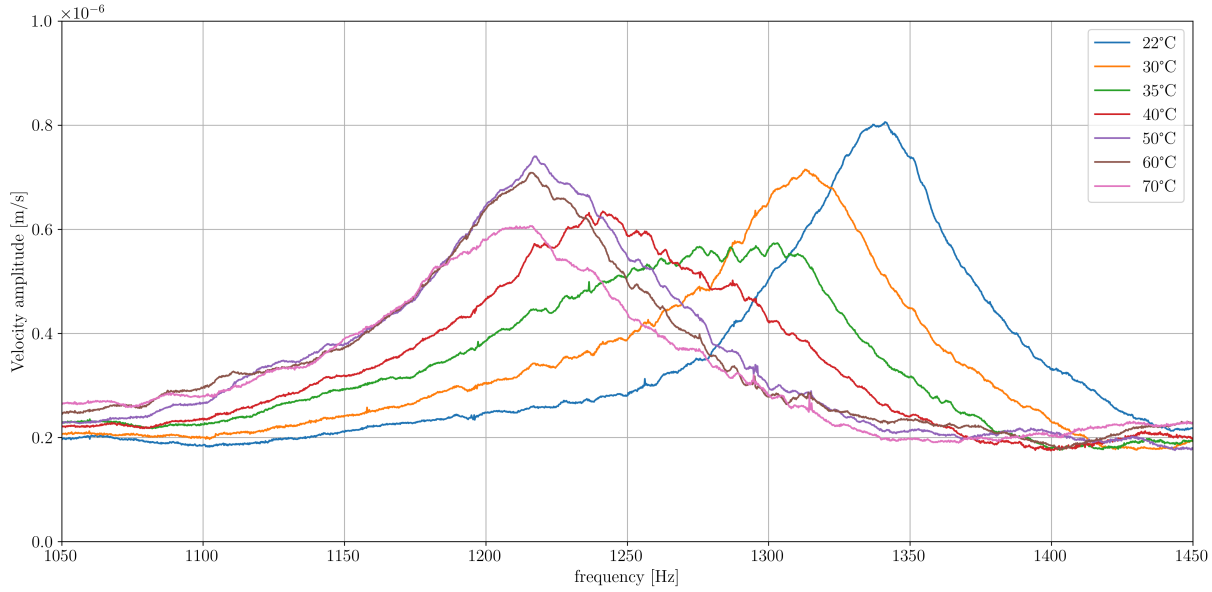

Figure 6.2: Temperature dependance of the (4,0) mode frequency

The results from the measurements are visible in **Figure 6.2**. They showed a strong temperature dependance of the motor (4,0) modal frequency on motor temperature, with the frequency at room temperature at 1370 Hz, at 35°C at 1280 Hz and at 50-60°C at 1240 to 1230 Hz. As the electromagnetic simulation does not provide us with continous results, a single discreet point needed to be chosen for the harmonic forcing, which should coincide with the motor normal frequency so that a resonance could occur At room temperature the (4,0) modal frequency is at 1370 Hz and 2568.75 rpm - a rotational speed that is not reached during motor operation. The electromagnetic forces calculated at the selected oper-

ating point of 1280 Hz as described in Section 5.1.7 were applied and the model was adjusted with the bearing shield springs to have the (4,0) mode at that frequency, as described in Section 5.1.5.

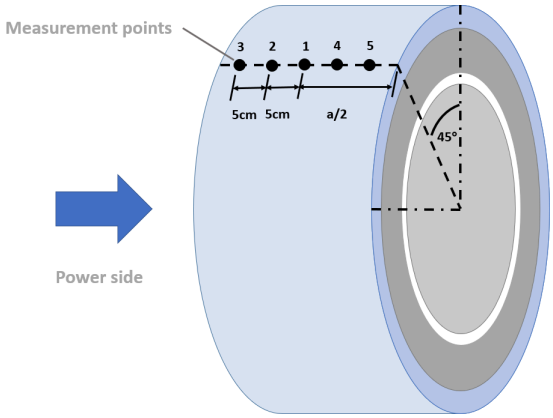

Figure 6.3: Positioning of mesurement points for motor running tests

6.1.2 Motor Running Tests

Motor running tests were then performed and the vibration amplitude and velocity were measured at 5 points across the motor surface, as shown in **Figure 6.3**. They were located at 45 degrees from the upper center part of the motor and were spaced 50 mm apart, with the first measurement points MP1 located in in the middle of the housing. This positioning was chosen to avoid cooling pipes and other equipment mounted on the motor, and to prevent proximity with the chosen absorber mounting locations, permitting consistent subsequent validation measurements. The laser vibrometer was pointed at those points in sequence, and the motor spun up externally from 0 to 2500 rpm, with an acceleration of 1 rad/sec^2 for all measurement points in series. An FFT was performed on each measurement using a Hanning window with 2/3 overlap and a Campbell diagram was obtained for every point, shown in **Figure 6.5**. It visualises the relationship between motor rotational speed and vibration frequency, with the velocity amplitude as colour. The velocity amplitude at the center of the motor, measured at MP1 was equal to 94.7 mm/s, and for the other points from MP2 to MP4 ranges from 63.1 mm/s to 104 mm/s.

Two notable effects could be observed. First, the velocity amplitude decreases from the middle of the housing surface towards the periphery. This is consistent with the motor geometry, the added stiffness contribution by the bearing shields and the locations where the electromagnetic forces act. Second - since the tests were conducted directly after each other, the motor temperature increases after every run, shifting the resonance frequency and reducing the vibration amplitude towards the lower end of the spectrum. Since the measurements for MP1 were conducted under the desired conditions, it served as a benchmark to establish the damping of the system.

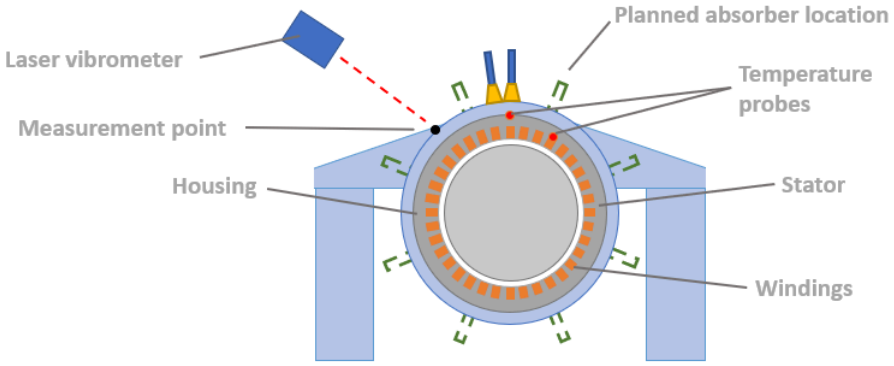

Figure 6.4: Motor running test measurement setup

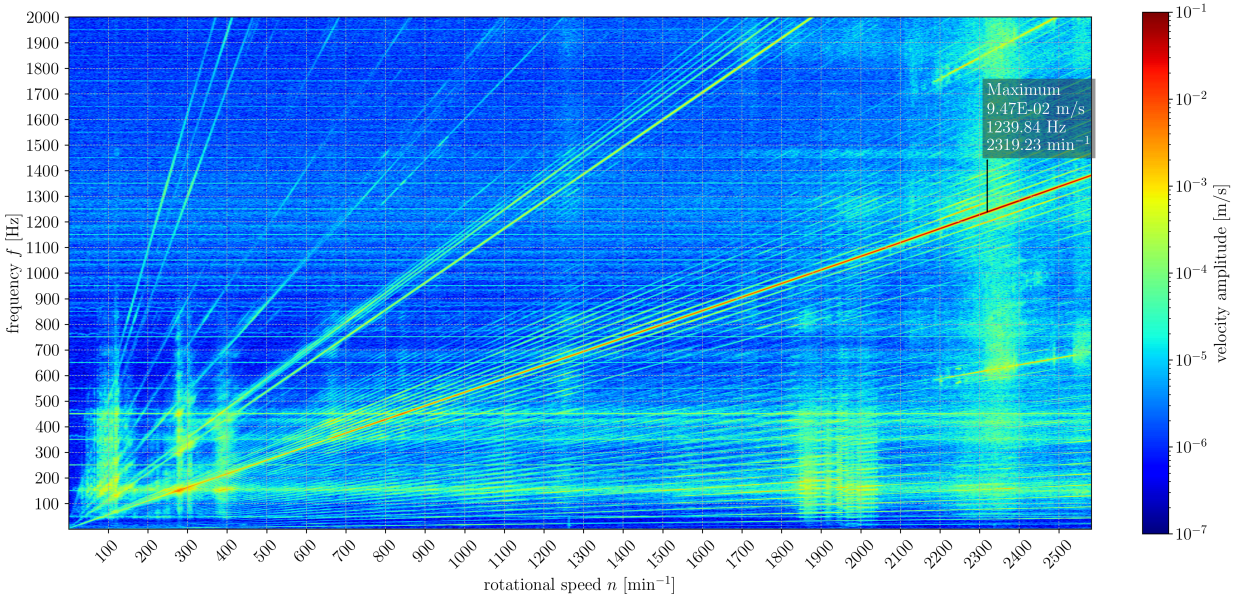

Figure 6.5: Campbell diagram for MP1

6.1.3 Linear Frequency Response

As the set of electromagnetic forces was calculated discretely for every work point an assumption was made that the magnitude and the vectors of the forces stay relatively constant in the small enough frequency range. As an example for a harmonic excitation at 2400 rpm, with a frequency of 1280 Hz the peak stator teeth force reached 313.3 N, and at 2100 rpm with a frequency of 1120 Hz a value of 305.8 N. This constituted a difference of about 2.5% over a range of 300 rpm and 160 Hz. Treating the forces as equal for all the frequencies in the 1150 Hz to 1450 Hz range would thus introduce a small error, which was deemed acceptable given the magnitude. Using the force calculated at 1280 Hz the error at resonance would be zero.

The state vector was computed for the first harmonic order and frequency response analysis was performed on the undamped motor without absorbers. The NlVib library was used as a

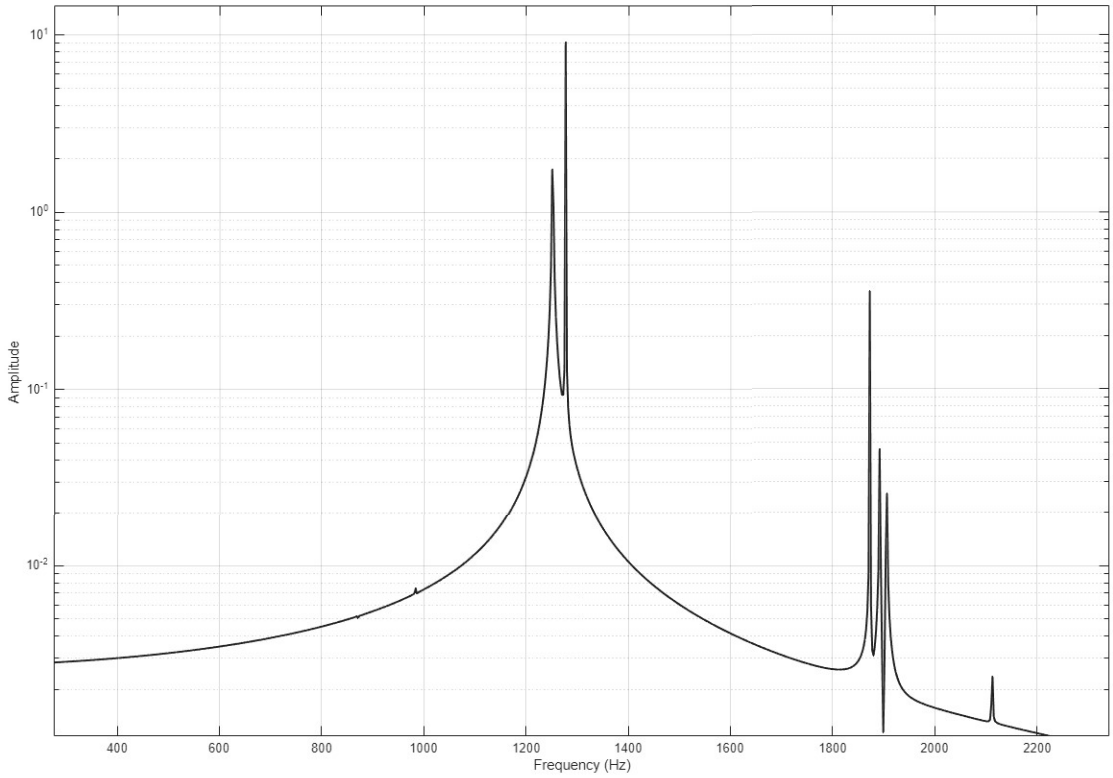

Figure 6.6: Linear frequency response curve at the node corresponding to MP1

linear solver, obtaining convergence in a single step. The reduced sine and cosine coefficients were extracted and projected into physical space following the reverse transformation:

$$c_{\text{red}} = X_{n+1:2n} \qquad s_{\text{red}} = X_{n+1:3n} \tag{6.1}$$

$$c_{phys} = T c_{\text{red}} \qquad s_{\text{phys}} = T s_{\text{red}} \tag{6.2}$$

The peak displacement amplitude was obtained as the residual sum of squares across all axes, and the velocity amplitude was calculated by multiplying the displacement with the frequency of the harmonic, giving us the peak results regardless of phase:

$$\hat{q} = \sqrt{\sum_j (c^2_{\text{phys},j} + s^2_{\text{phys},j})} \tag{6.3}$$

$$\hat{\nu} = \omega \sqrt{\sum_j (c^2_{\text{phys},j} + s^2_{\text{phys},j})} \tag{6.4}$$

The frequency response for the node corresponding to MP1, when excited by a unit force with an equivalent vector field, is visible in **Figure 6.6**. In an undamped motor excited by a harmonic force at 1280 Hz - at resonance, the vibration amplitude reaches a peak value of 2779.02 µm with a velocity of 22167.3 mm/s. Those values are unrealistic as an average value of 87.26 mm/s was measured with the laser vibrometer, but easily explainable - the system is completely undamped. The values do not reach infinity simply due to the inherent damping from the FEM solver itself [11] or because the frequency for which the values are calculated were not perfectly in resonance. Thus to be able to properly calculate absorber effectiveness, system damping needed to be introduced.

The presence of two response peaks at the resonance frequency should also be noted. They correspond to the degenerate (4,0) mode pair described in Section 5.1.5, whose slightly offset frequencies arise from FEM discretisation as explained in Section 2.2.

6.1.4 Proportional Damping

By using Rayleigh damping, the damping matrix $\boldsymbol{D}$ was build as proportional to the linear combination of the mass and stiffness matrices $\boldsymbol{M}$ and $\boldsymbol{K}$. The mechanism and can be defined by the equation:

$$\boldsymbol{D} = \alpha \boldsymbol{M} + \beta \boldsymbol{K} \tag{6.5}$$

where α and β are the damping coefficients.

They were determined following the approach outlined in [12], with a linearly increasing target damping ratio across the frequency band of interest. First the eigenmodes of the structure were calculated and the damping ratio was anchored to the first and last significant mode of the system. For the current case those were chosen at 1190 Hz and 1450 Hz. The linear target was calculated based on Eq. (6.6) and three damping coefficient pairs were computed — one anchored at the first and the last significant modes, one extended to 2.5 times the significant mode number, and one taken as their average.

$$\zeta_i = \zeta_i + (\zeta_m - \zeta_1) \cdot \frac{\omega_i - \omega_1}{\omega_m - \omega_1} \tag{6.6}$$

The pair with the best resulting damping curve was selected. The damping ratios ζ_i at the corresponding modes were adjusted until a value for velocity and deformation matching the ones from the measurements were reached. The damping coefficients were then calculated as:

$$\zeta(\omega_i) = \frac{\alpha}{2\omega_i} + \frac{\beta\omega_i}{2} \tag{6.7}$$

Thus an α of 482.5 and β of 7.46e-06 were calculated with ω_i as the respective mode's frequency. This resulted in a deformation velocity for the node equivalent to MP1 of 106.281 mm/s. For the motor with mounted absorbers the damping was applied exclusively to the interior degrees of freedom of the substructure. The degrees of freedom, where the nonlinear elements are to be generated, were intentionally left undamped. This prevented double-damping and preserved the physical consistency of the nonlinear coupling. The damping matrix D was built and projected into the reduced space to $\boldsymbol{D}^{\text{red}}$ simular to the other system matrices as described in Section 2.4.3.

6.2 Frequency response with DVA

With the validated baseline established, the dynamic vibration absorber arrays were introduced into the simulation model as nonlinear friction elements. A convergence study was performed to ensure numerical accuracy of the nonlinear solver. Frequency response graphs for varios normal forces applied on the absorbers were calculated to find the setting leading to the biggest amplitude and velocity reduction, while also taking into account the frequency shift from the damping effects.

6.2.1 Convergence Tolerance

To determine what minimum value for the Newton-Raphson residuum was needed to obtain an accurate result, an amplitude frequency response from 1150 Hz to 1450 Hz was performed for two different cases of harmonic forcing. The study was conducted with a harmonic order of H = 1, since the exported forcing contains just a single harmonic component at the motor resonance frequency. The first set had the full physical magnitude, and the second set had its values normalised, but the vectors retained. A Newton-Raphson damped step size of 0.05 with 64 time steps per period were selected empirically to ensure robust convergence. The damping matrix D^{red} obtained in Section 6.1.4 was applied. The normal force applied to both absorbers was varied from 1 N to 1200 N and the convergence criterion value was swept from 1E-01 to 1E-08.

For both cases it was determined that the convergence tolerance was practically independent from the applied normal force. With unit forcing convergence can be obtained at tolerance of 1E-04 with 136 iterations per frequency point needed on average. For the physical force a fully converged value can be obtained at a residuum of 1E-02 with an average of 209 iterations per point. A convergence tolerance of 1E-04 was adopted for all subsequent analyses to ensure accuracy across all investigated force levels.

6.2.2 Friction Interface Analysis

The tangential contact stiffness and friction parameters were derived in Section 5.1.4. For the aluminium-steel interface at $F_N = 100N$, the combined tangential stiffness was found to be $k_t \approx 4.6 \times 10^7$N/m, with a relative displacement amplitude for sliding at a single Jenkins element equal to 0.0073 µm. The relative displacement between the fixed and moving friction plates from the nonlinear solution was found to range from 26.65 to 328.12 µm across all elements, meaning that the friction interface operates in deep gross slip throughout the entire investigated range. In gross slip regime the Jenkins element force reduces to a purely velocity-dependent form, contributes no stiffness to the system and is equivalent to added viscous damping:

$$f_{nl}(t) = \mu F_N \cdot \dot{u}_{rel}(t) \tag{6.8}$$

The DVA working mechanism requires a stiffness coupling between the absorber mass and the primary structure. In gross slip this coupling is absent, and the absorber mass oscillates without a restoring spring. As a consequence, the frequency response under physical contact conditions shows monotonic amplitude reduction with increasing normal force. This result is consistent across all three absorber configurations and leads to an unrealistic representation of the effectiveness of the absorbers.

This finding is a direct consequence of the contact geometry. In the aluminium-steel interface with $A_c = 720\text{mm}^2$ and $\text{Ra} = 0.8\mu\text{m}$, the contact stiffness is too high relative to the achievable friction force for partial slip to occur at the relative displacements present at the friction nodes. For the purpose of evaluating the performance of the designed array, a constant $k_t \approx 1.2 \times 10^6$N/m was applied per damper for the subsequent study, with recommendations for a redesign discussed in Section 8.2.

6.2.3 Normal Force Parametric Study

Three absorber configuration were explored. In the first configuration both absorbers were perfectly tuned to the resonance frequency of 1280 Hz, representing an ideal single frequency absorber. In the second the two absorbers were slightly mistuned in regard to the resonance frequency to 1307.4 Hz and 1249.9 Hz respectively, forming the designed split-array configuration. In the third, where both absorbers were tuned to 1370 Hz, representing a mistuned case. The applied normal force F_N was varied for each individual damper from 0 to 500 N, with equal normal force for both absorbers in the cases where they share a tuning frequency. The frequency response was evaluated for the node corresponding to MP1 between 1150 Hz and 1750 Hz, encompassing both the original resonance peak and potential shifts.

The velocity at the motor housing for the first case is visible in **Figure 6.7**. As F_N increases toward the optimum value, the Jenkins element stiffness contribution activates the DVA

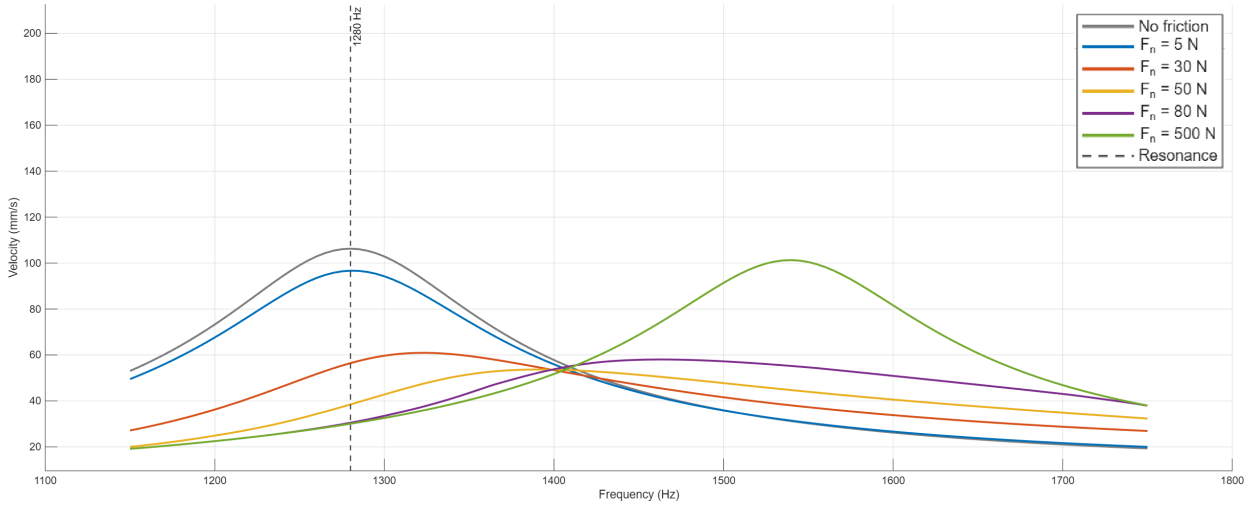

Figure 6.7: Velocity frequency response curve with precisely tuned absorbers

mechanism. Rather than producing the classic double-peak anti-resonance structure characteristic of a lightly damped primary system, the response shows a progressive reduction and broadening of the motor resonance peak. The structural damping present in the moderately damped motor model is sufficient to suppress the formation of distinct anti-resonance notches, instead distributing the absorbed energy over a broader frequency range. The peak velocity amplitude at 1280 Hz decreases from 106.28 mm/s in the frictionless case to 53.63 mm/s at the optimal normal force $F_{N,opt} = 50$ N, a reduction of 50%, accompanied by a measurable broadening of the response by approximately 200 Hz, while simultaniously shifting the maximum amplitude to 1385 Hz. At $F_N = 500$ N the interface is in locked regime and the response peak shifts to 1540 Hz with a velocity of 101.29 mm/s, confirming that the locked Jenkins spring stiffness detunes the absorber from the motor resonance as expected.

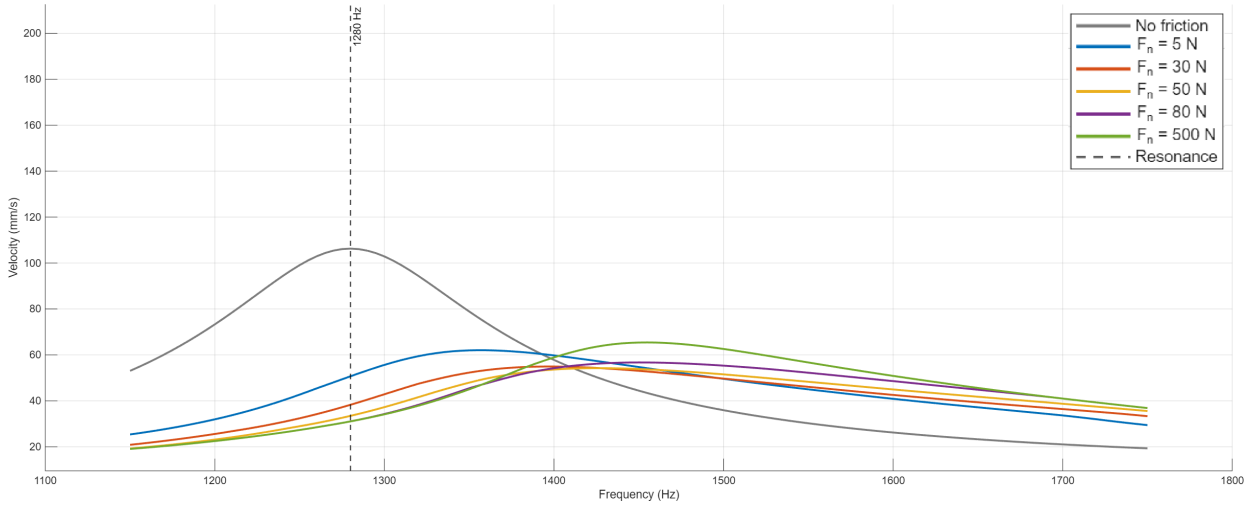

Figure 6.8: Velocity frequency response curve with the mistuned absorber array concept

In **Figure 6.8** the velocity from the frequency response sweep for designed split-array configuration is seen, with the heavier absorber tuned to its ideal normal force of 70 N and the lighter one shown with different normal forces. In the perfectly tuned case with $F_{N,optA} =$

50 N applied to the 1307.4 Hz absorber and $F_{N,optB} = 70$ N to the 1249.9 Hz absorber, the maximum velocity amplitude at 1280 Hz decreases from 106.28 mm/s by 49% to 54.2 mm/s, with a shift of the peak frequency to 1425 Hz. As the lower absorber force moves into the locked state at $F_N = 500$ N the response peak shifts to 1455 Hz the attenuation continues to be substantial with a velocity of 65.4 mm/s. When the normal force for the mistuned absorber arrays is varied in tandem, their behaviour closely resembles that of the perfectly tuned case. With the $F_N = 50$ N at 1385 Hz the velocity is equal to 53.53 mm/s In the locked regime the system's response peak shifts to 1540 Hz at 101.28 mm/s.

The mistuned configuration, with both arrays tuned to 1370 Hz, confirms the sensitivity of the DVA solution to tuning accuracy. In the optimal case at $F_N = 20$ N,the peak amplitude at the motor resonance frequency is shifted to 1300 Hz reduced by only 19% to 85.74 mm/s. Its frequency response can be seen in **Figure 6.9**.

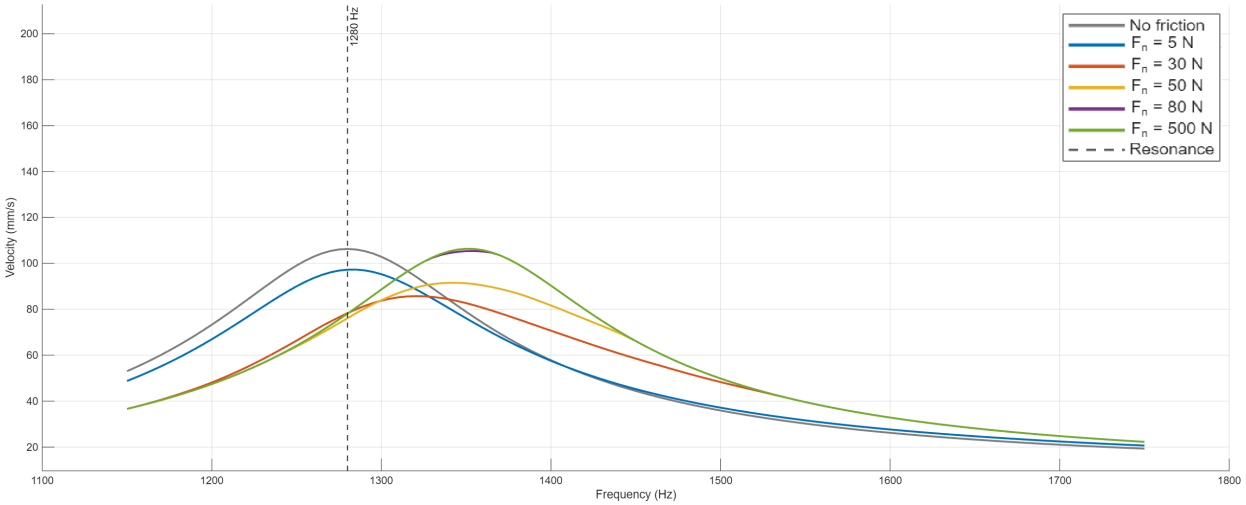

Figure 6.9: Velocity frequency response curve with the purposely mistuned absorbers

7 Discussion of the Results

This chapter reflects on the methodology, results, and limitations of the present work. It evaluates whether the chosen approach was successful, where results differed from expectations, and what consequences follow for the design aprocess.

7.1 Simulation Framework

The simulation framework developed in Section 5.1 successfully captures the modal behaviour of the motor with acceptable accuracy. The calibrated FE model reproduces the experimentally measured (4,0) at 22°C mode frequency within 0.15%, with the degenerate pair frequencies bracketing the measured value of 1370 Hz. The Rubin reduction preserved eigenfrequency accuracy for the frequency range of interest. The assumption of constant electromagnetic force magnitude across the frequency range of interest introduced a maximum error of 2.5%, which was deemed acceptable. The linear harmonic analysis in Section 6.1.3 produces a baseline velocity response that, once Rayleigh damping is applied, agrees with the laser vibrometer measurements within acceptable margins. This demonstrates that the simulation reproduces the physical motor behaviour with acceptable fidelity.

7.2 Absorber Design and Effectiveness

The absorber array design successfully achieved the target frequency range of 1059.3 to 1374.3 Hz across 13 configurations, and the simplified simulation model reproduced the full absorber modal behaviour with an average error of 0.85%. The parametric study demonstrated that under simulation conditions representing a partial slip friction interface the absorber array concept is effective in principle and in simulation. The split-array configuration showed the most favourbale behaviour and was selected as the recommended design due to its combination of effectiveness and robustness. The investigation of the mistuned configuration confirmed the sensitivity of effectiveness to tuning accuracy.

The contact mechanics analysis in Section 6.2.2 revealed a critical limitation of the current design. The calculated combined tangential contact stiffness was found to be too high relative to the achievable friction force at the displacements present at the friction nodes. This lead

to the absorber operating in deep gross slip throughout the entire investigated normal force range, eliminating the coupling mechanism that underpins its effectiveness. The physical absorber in its current form therefore can not achieve the intended vibration reduction.

This finding was not anticipated during the design phase and represents the central limitation of the current implementation. It is however a correctable design constraint rather than a fundamental barrier. Reducing the contact area would increase the nominal contact pressure for a given normal force, shifting the partial slip threshold to lower displacement amplitudes. Alternatively, introducing a thin soft interlayer between the friction surfaces would reduce the combined tangential contact stiffness, achieving partial slip without geometric redesign of the existing components. This verification step, checking the operating friction regime before manufacturing, is the most important methodological recommendation arising from the present work.

7.3 Assessment of the Design Process

Beyond the specific results, the present work revealed a critical dependency in the predictive design workflow. The received electromagnetic excitation showed that the strongest vibration in physical motor operation at room temperature occurs at a frequency that does not coincide with the structural (4,0) resonance frequency at 1370 Hz. Additionally the theoretical resonance at 1370 Hz occurs at a rotational speed outside the motor's operational range. Thus for future work it is recommended that the excitation frequency must be established as the first input to the absorber design process, before structural resonance targets or tuning ranges are defined. The scope of the work was consequently adjusted to evaluate the arrays' effectiveness at the structural resonance condition, which remains the technically correct target.

7.4 Experimental Status

The damper arrays were physically manufactured and mounted on the motor, with the test infrastructure in place. Experimental validation was not completed within the thesis timeline due component delivery encountered significant delays, pushing the deadline for completing the experiments into the future. The experimental validation remains the immediate next step for this work and will provide the definitive assessment of absorber array effectiveness, once the contact interface has been redesigned and the dampers retuned to the correct operating frequency.

[1]

[1] Initial draft generated by Claude (Anthropic, 2026), subsequently revised by the author. [4]

8 Conclusions and Future Work

The present thesis investigated the predictive design of a tuned friction damper array for reducing electromagnetically excited radial vibrations in an existing Permanent Magnet Synchronous Motor. The work was motivated by the growing relevance of electric motor NVH in electrified transportation and the absence of established predictive design workflows for friction-based passive damping solutions targeting specific motor resonances.

8.1 Summary and Conclusions

A complete simulation pipeline was developed and validated — comprising a calibrated reduced-order finite element motor model, a simplified absorber model, and a nonlinear harmonic balance analysis framework. The simulation reproduces the measured motor modal behaviour within 0.15% and the vibration amplitude at all measurement points with acceptable accuracy, confirming the reliability of the predictive approach. Under simulation conditions representing a partial slip friction interface, the designed absorber arrays achieve up to 50% reduction in peak housing velocity at the motor resonance frequency, with the mistuned split-array configuration providing the best combination of effectiveness and robustness across the investigated frequency range.

It was determined that friction dynamic vibration absorber array can be designed predictively for an existing PMSM using the methodology demonstrated here. The developed framework is accurate, validated, and directly reusable for other motor configurations. The developed friction damper is effective in simulation but requires physical modifications before experimental effectiveness can be demonstrated.

Two findings emerged beyond the primary design objective that carry broader significance. First, the physical friction interface as manufactured operates in deep gross slip rather than partial slip, eliminating the DVA stiffness coupling mechanism. This finding underscores that operating friction regime verification is a necessary step in any friction DVA design process. Second, the electromagnetic excitation frequency at the motor's strongest physical vibration condition does not coincide with the structural resonance frequency targeted by the absorber design. This identifies that the definition of structural damping targets in any future motor NVH programme should include the frequency of the electromagnetic forcing as a critical process variable.

8.2 Recommendations

Before experimental validation is attempted the friction contact area should be reduced or a a thin copper interlayer should be added between the friction surfaces to shift the interface into the partial slip regime at the operating displacement amplitudes. The leaf spring fasteners should be replaced with tighter-tolerance alternatives to eliminate the play identified at the attachment points. The current clearance introduces variability in the effective leaf spring boundary conditions that compromises both the absorber frequency tuning and the validity of the revolute joint assumption in the simulation model. The damper arrays should be retuned accordingly using the mass plate adjustment procedure described in Chapter 4. The normal force parametric study should then be repeated for the corrected tuning configuration.

8.3 Future Outlook

Once the experiments are conducted using the measurement process established in Section 6.1 a definitive assessment of absorber arrays' effectiveness under physical operating conditions will be provided. Beyond the immediate validation, the temperature dependence of the motor resonance frequency represents a fundamental challenge for fixed-frequency tuned passive absorbers. A semi-active variant of the present design, capable of adjusting the absorber tuning frequency through controlled adjustment of the absorber parameters could substantially improve effectiveness across the full operating range. The simulation framework developed in this thesis is directly applicable to other PMSM configurations and represents a validated, reusable tool for future motor NVH programmes. Extension to motors with different slot-pole combinations, different resonance modes, or different operating speed ranges would further establish the generality of the predictive design approach demonstrated here.

[1]

[1] Initial draft generated by Claude (Anthropic, 2026), subsequently revised by the author. [4]

A Concept Selection Scoring Matrices

The following scoring matrices document the trade-off analyses conducted in Section 4.1 to select the most suitable vibration reduction concept and energy dissipation mechanism. In the first analysis, presented in **Table A.1** and **Table A.2**, a wide set of vibration reduction concepts was assessed across eight criteria grouped into four categories: performance, system requirements, integration, and sourcing. In the second analysis, presented in **Table A.3**, candidate energy dissipation mechanisms were evaluated against three weighted criteria: performance, robustness, and ease of integration.The assigned weights reflect the design constraints and priorities established in Section 4.1. The matrices are included here for transparency and reproducibility of the decision-making process.

Table A.1: Vibration reduction concept scoring – Performance and System Requirements

	Performance		System Requirements		
Method	Effectiveness	Bandwidth	Power	Control	Subtotal
Weight	*0.125*	*0.125*	*0.125*	*0.125*	*0.50*
Motor Encapsulation	2	4	5	5	2.000
CFRP Frame	3	2	5	5	1.875
Conventional DVAs	4	3	5	5	2.125
MR Dampers	4	3	2	4	1.625
EM Dampers	4	4	2	3	1.625
Shunted Dampers	3	4	4	5	2.000
Piezoelectric Patches	4	4	4	4	2.000
Piezoelectric Actuators	5	5	1	2	1.625

Table A.2: Vibration reduction concept scoring – Integration, Sourcing and Final Score

	Integration		Sourcing		
Method	Mass	Difficulty	Cost	Availability	Final Score
Weight	*0.125*	*0.125*	*0.10*	*0.15*	*1.00*
Motor Encapsulation	4	5	5	5	4.375
CFRP Frame	3	1	1	3	2.925
Conventional DVAs	5	4	5	5	4.500
MR Dampers	3	2	3	3	3.000
EM Dampers	4	2	3	3	3.125
Shunted Dampers	4	3	4	3	3.725
Piezoelectric Patches	5	1	2	2	3.250
Piezoelectric Actuators	2	1	1	3	2.550

Table A.3: Energy dissipation mechanism selection scoring matrix

Method	Performance	Robustness	Integration	Final Score
Weight Coefficient	*0.35*	*0.30*	*0.35*	*1.00*
Cylindrical Friction	4	3	4	3.70
Slotted Bolted Plate	5	4	3	4.00
Rubber Damper	2	2	4	2.70
Particle DVA	3	4	3	3.30
Pall Friction Damper	4	4	3	3.65
Stockbridge Damper	3	4	2	2.95
Beam Damper	2	5	2	2.90

B Material Parameters

The material parameters used in the simulation models are compiled in the following tables, together with their respective sources. The values are given at room temperature.

Table B.1: Material properties of all model components

Component	Material	ϱ (kg/m^3)	E (MPa)	ν (-)	G (GPa)	Source
Stator	M270-35A	7650	200	0.30	76.92	[1]
Stator, Winding	Varnish	850	3.2	0.25	1.28	[9]
Winding	Copper	8900	110*	0.34	41.04	[38]
Housing, Absorber	EN AW-6060 T6	2700	69.5	0.33	–	[61]
Absorber	S235JR+AR	7850	212	0.30	–	[62]
Leaf Springs, Fasteners	C45	7700	210	0.30	–	[54]
Leaf Springs, Fasteners	Loctite EA 9497	–	52.6	–	0–	[25]

Table B.2: Resulting orthotropic material properties used in the FEM model

Component	ϱ (kg/m^3)	E_x (GPa)	E_y (GPa)	E_z (GPa)	ν_{xy} (-)	ν_{yz} (-)	ν_{xz} (-)	G_{xy} (GPa)	G_{yz} (GPa)	G_{xz} (GPa)
Stator Core	7310	49.08	190.16	190.16	0.30	0.26	0.26	19.45	73.14	19.45
Winding	4875	56.60	6.22	6.22	0.20	0.24	0.20	1.29	21.16	21.16

* annealed, cold-formed 130 MPa

C Mesh Convergence Study

C.1 Absorber model

For the full absorber model the mesh generation was conducted automatically by the ANSYS Mesh generator with program controlled element order and mechanical physics preference. The element size was varied from 5 to 0.5 mm separately for the leafsprings, as the components with the biggest influence on the structure's stiffness, and for the entire rest of the assembly. The values for the first 4 modal frequencies are tracked, and can be seen in **Figure C.1**. No significant variation was observed for any of the components. A convergence threshold of 3% change relative to the finest element size was adopted. Following the results an element size of 1 mm was adopted for the leaf springs, as the coarsest size at which all tracked frequencies remained within this threshold, and 5 mm for all other components.

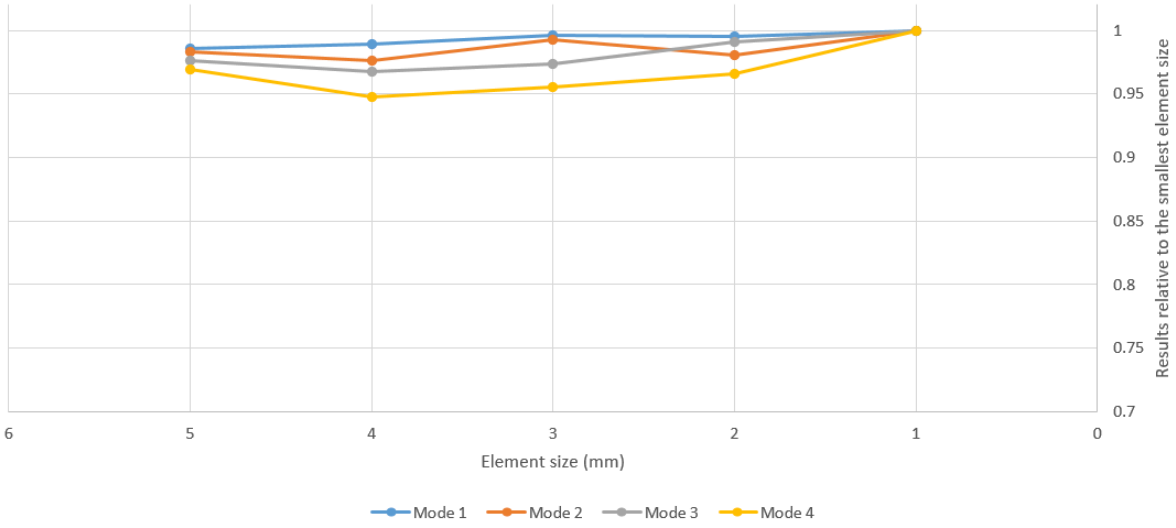

Figure C.1: Convergence of the modal parameters for the absorber

C.2 Motor model

For the motor model additional mesh modifications to the boundary faces described in Section 5.1.3 was introduced. The mesh for the housing was generated with hexahedral elements, with tetrahedral elements used only where necessary to improve convergence behaviour [11].

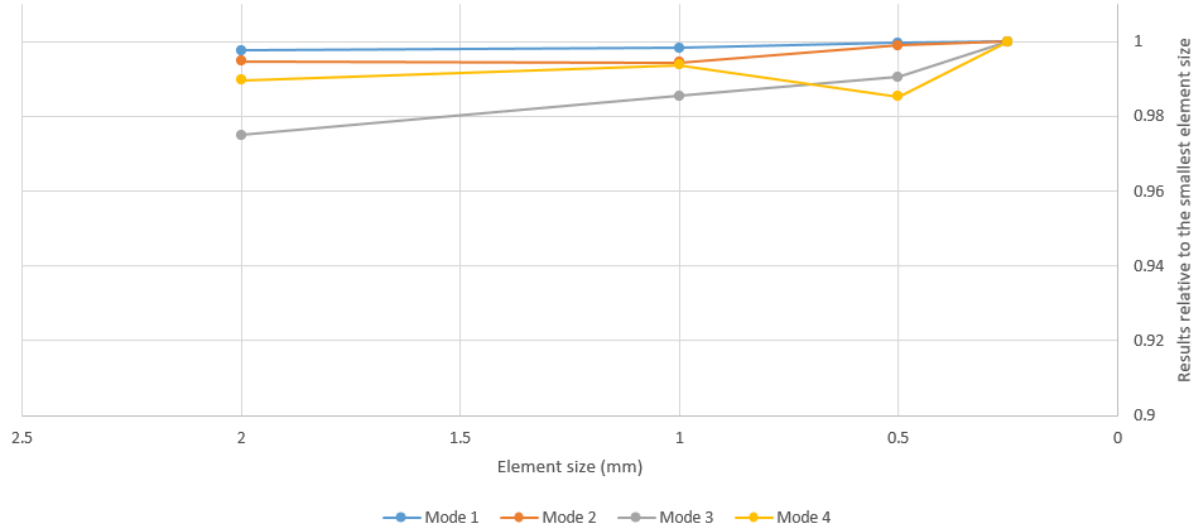

Figure C.2: Convergence of the modal parameters for the leafsprings

The element size of each single component was varied from 25mm to 3mm, while all other components within the assembly were meshed with 5mm element size. This ensured that only the element size of the investigated component had influence on the results. Beyond an element size of 3mm the degrees of freedom count and computational requirements grew exponentially, thus making further mesh refinement impractical.

Static and modal simulations were conducted in this manner for the housing, stator, and windings separately. As the modal characteristics of the model were of particular interest, the natural frequencies of the entire assembly for multiple modes across all harmonic indices were recorded. To ensure good correlation between the modal shapes of the tracked modes, the Modal Assurance Criterion was calculated between the investigated modes for a particular element size and a common reference set of modal shapes [50]. A matrix indicating the consistency between the mode shapes is formed, with values from 0 to 1 corresponding to the similarity between the mode shapes [50]. A MAC value of 0.3 served as a matching threshold.

As a secondary set of parameters the average total deformation, the average equivalent stress and the total strain energy for each component from the static simulation were also tracked. Although their values were not of particular importance for accurately modeling the structure's resonance behaviour, they proved useful as additional datapoints for determining result independence, as in the present study it was observed that static parameters converge slower than modal frequencies.

The parameter change for both the static and the modal simulations were plotted against the node count for all components. A threshold of 3% difference relative to the values at the smallest element size was adopted as the convergence criterion, in line with standard engineering practice. For the motor housing an acceptable convergence of all tracked modal frequencies was observed at an element size of 10mm. For the static parameters this level of convergence is visible across the board at an element size of 7mm. For the winding the

convergence of the modal frequencies can be observed at a much earlier point with an element size of 20mm. The behaviour of the static parameters however is much less ideal, reaching a maximum value of 2.8% for all parameters relative to those at the finest mesh, at an element size of 5mm. For the motor stator the modal frequencies have already converged at an element size of 20mm, with the average total deformation and the total strain energy reaching the threshold at an element size of 15mm.

Two additional observations regarding the stator element size however warrant mention. First the behaviour of the average equivalent stress values in the stator static parameter convergence plot can be described as unusual, experiencing a strong spike away from the finest parameters at an element size of 10mm, before later reaching the threshold of 3% difference from the finest element size values. As this phenomenon is only observed for the equivalent stress and can be caused by mesh transition effects at that element size, it was considered insignificant. Second, at an element size beyond 10mm for the stator, the automatic mesh generation algorithm of ANSYS Mechanical creates an unequal number of nodes on different stator teeth. As this would introduce problems at a later point, when applying the loading from the electromagnetic forces to the stator teeth, an element size bigger than 10mm was deemed unacceptable.

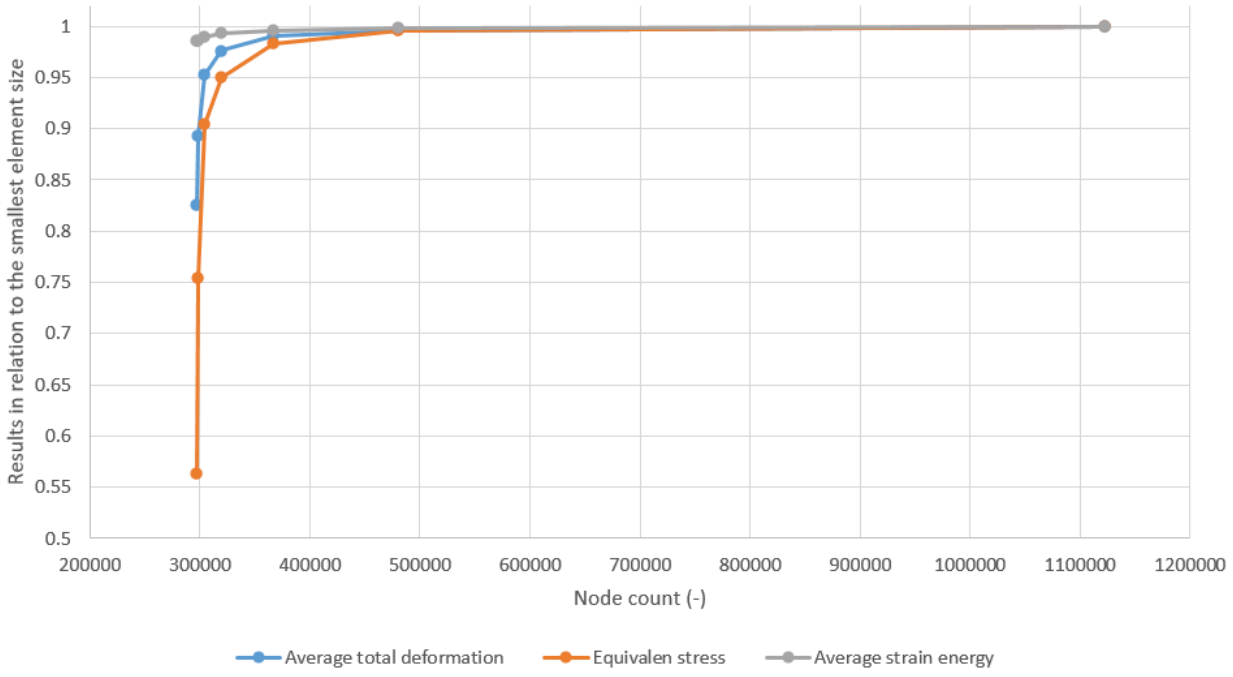

Figure C.3: Convergence of the static parameters for the motor housing

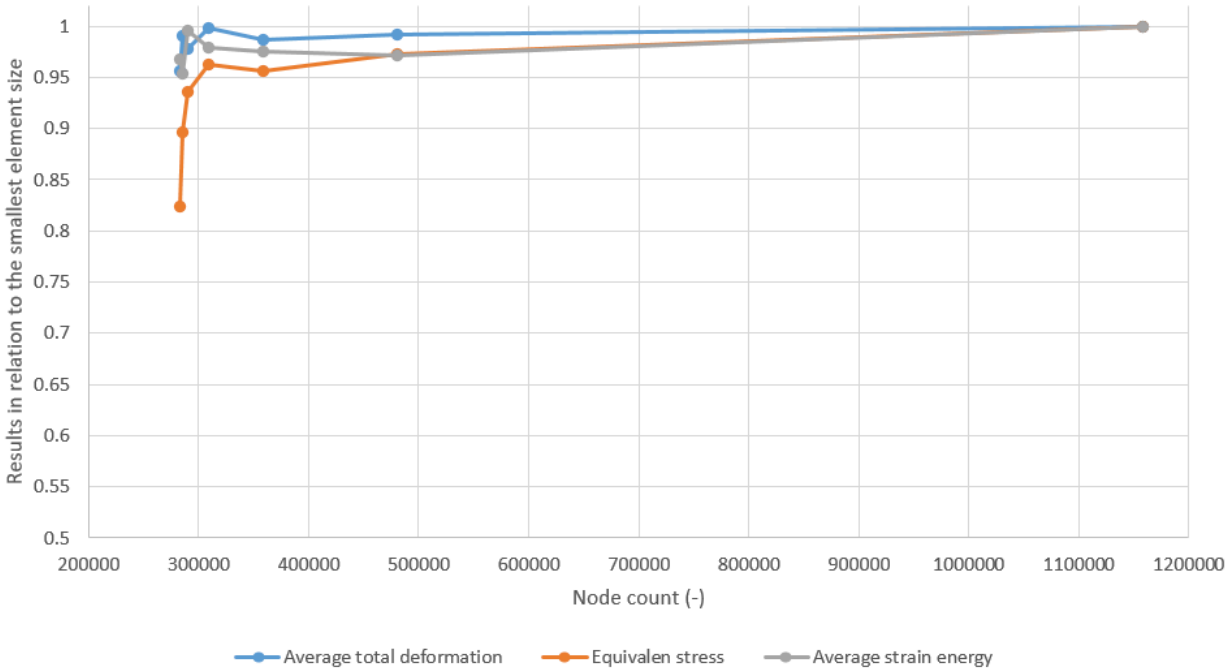

Figure C.4: Convergence of the static parameters for the motor winding

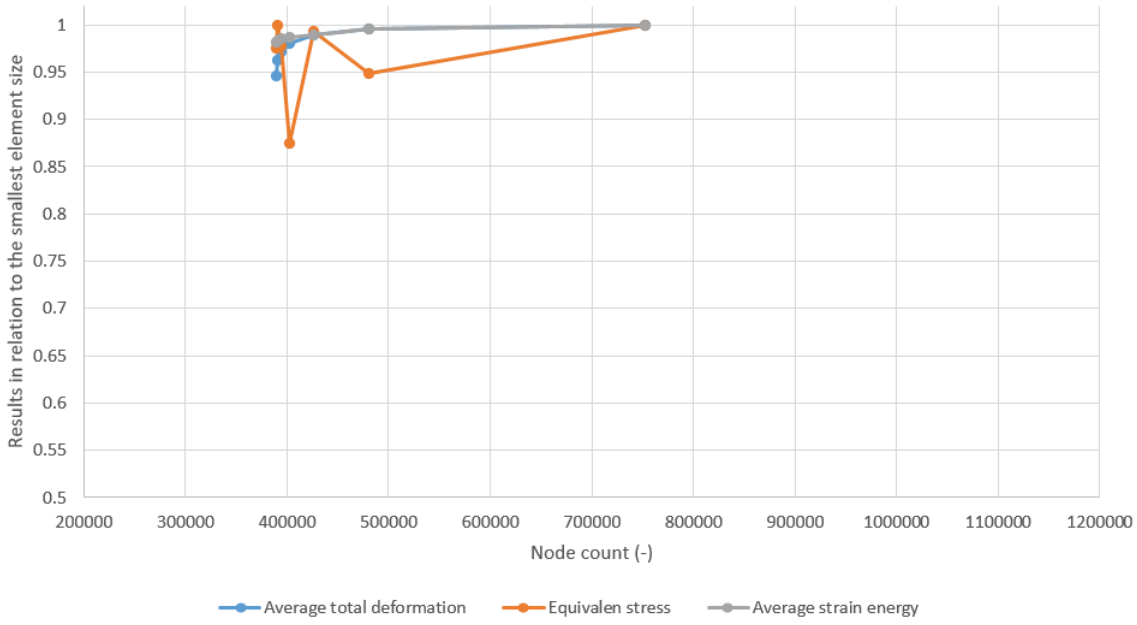

Figure C.5: Convergence of the static parameters for the motor stator

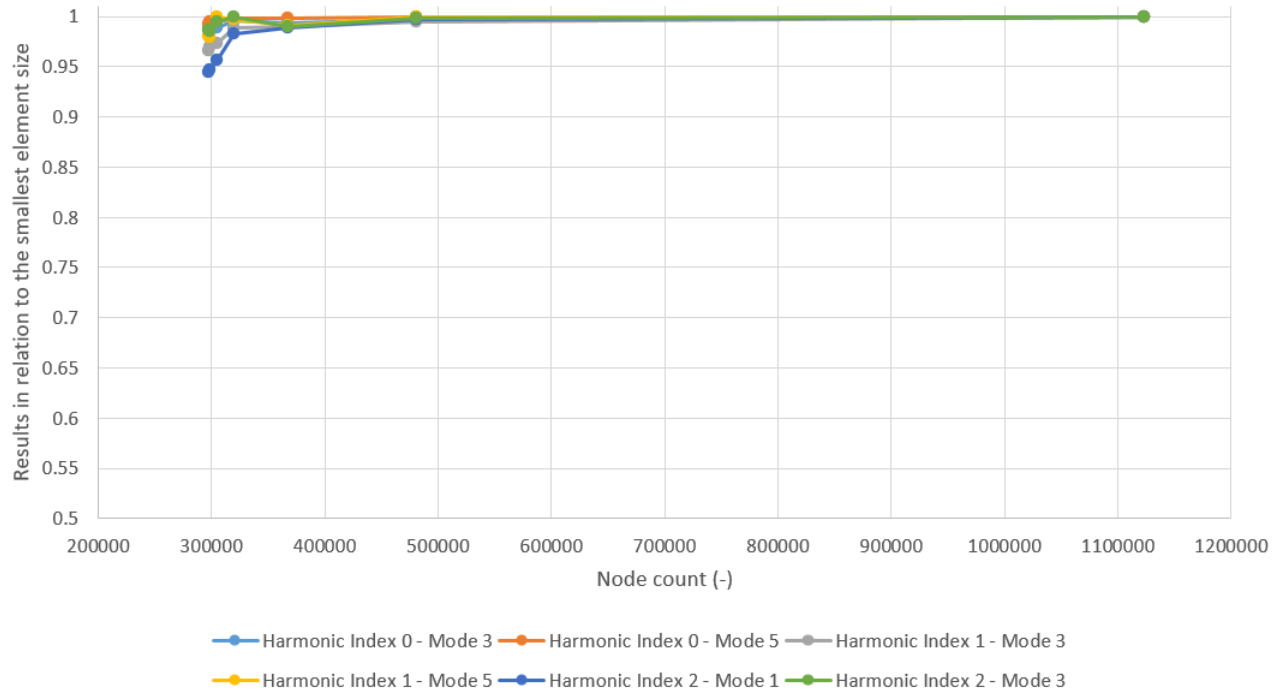

Figure C.6: Convergence of the modal parameters for the motor housing

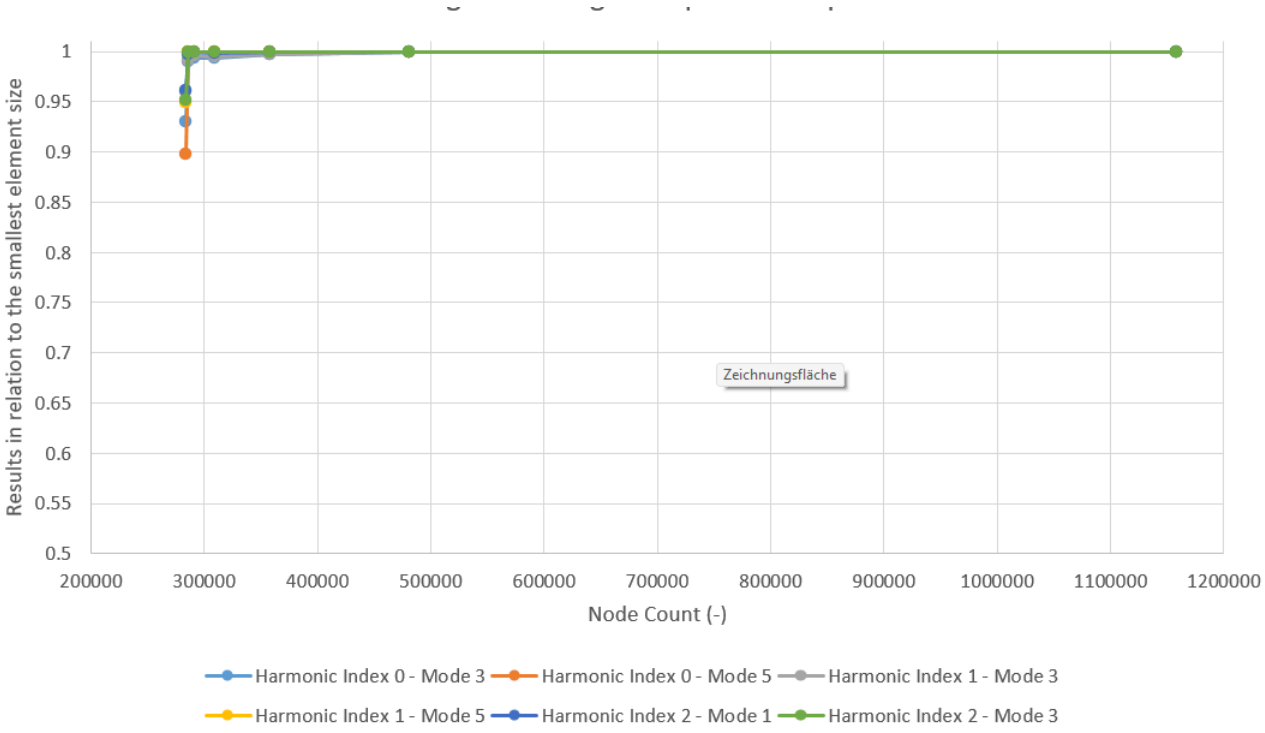

Figure C.7: Convergence of the modal parameters for the motor winding

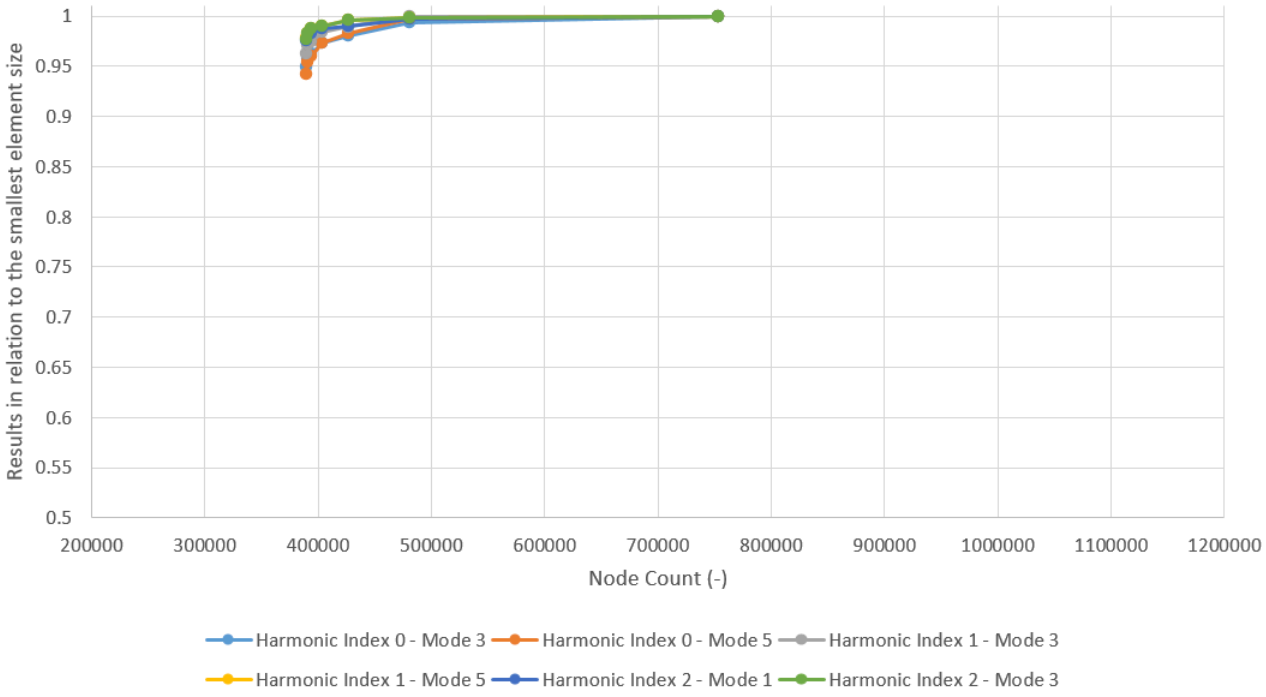

Figure C.8: Convergence of the modal parameters for the motor stator

D Absorber Frequency Tuning

The following table documents the frequency tuning of the dynamic vibration absorbers and the corresponding weight plate configurations used to achieve the target frequencies. The tuning was carried out as described in Section 4.3 and the values are included here for completeness and to allow reproducibility of the experimental setup.

Table D.1: DVA frequency tuning configurations and simplified model densities

No. Weight Plates	Moving Mass (g)	Frequency (Hz)	Simplified Model Density (kg/m^3)
0	102.81	1374.3	2134.84
1	114.57	1307.4	2379.05
2	120.28	1282.3	2497.51
3	126.96	1249.9	2636.31
4	132.67	1227.0	2754.77
5	138.37	1202.4	2873.23
6	145.06	1177.8	3012.07
7	150.77	1158.2	3130.53
8	156.47	1138.6	3248.99
9	163.16	1120.2	3387.80
10	168.86	1093.8	3506.26
11	174.57	1076.6	3624.72
12	180.27	1059.3	3743.18

E Spring Tuning

The tuning graphs of stiffness values for the linear springs of the dynamic vibration absorbers and the bearing shield springs are presented in **Figure E.1** and **Figure E.2** respectively. In both cases the spring stiffness was iteratively adjusted until the simulated modal frequencies were matched to the target values across the investigated configurations, as described in Chapter 5.

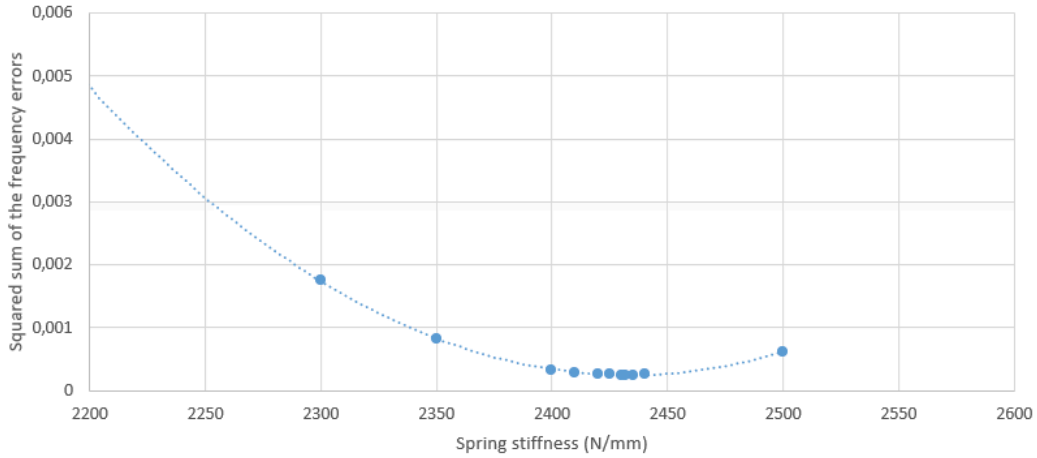

Figure E.1: Tuning the linear springs of the simplified dynamic absorber

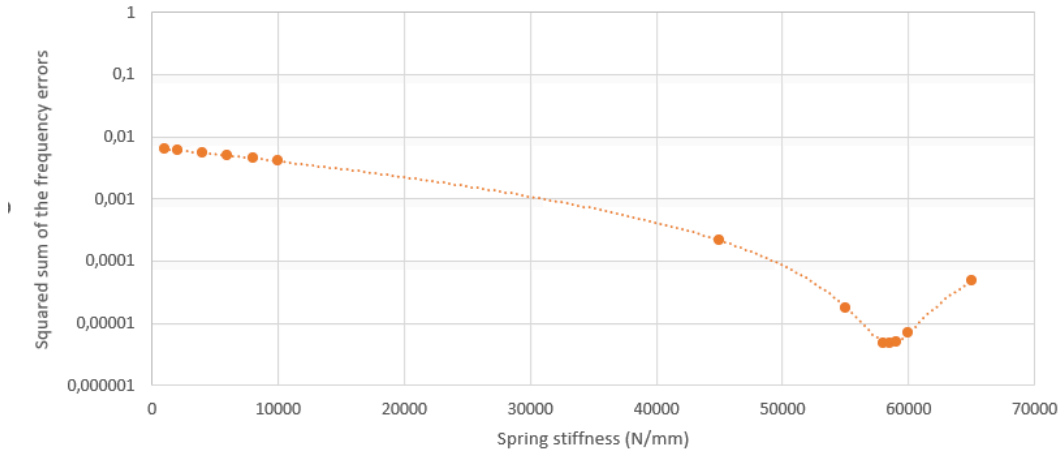

Figure E.2: Tuning the linear springs of the simplified motor section

F Technical Drawings

Änd. Ziffer	Feld	Datum	Geaendert	Genehmigt	Beschreibung der Aenderung und Aenderungsterminschluessel

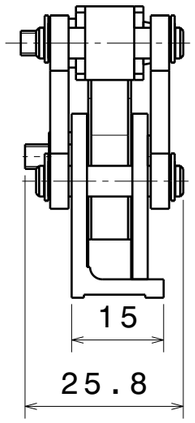

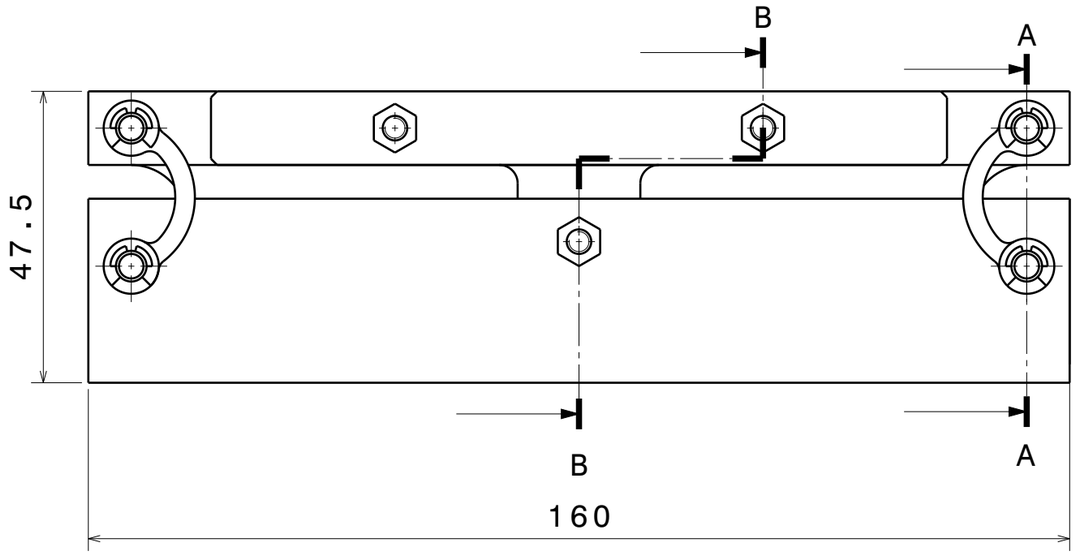

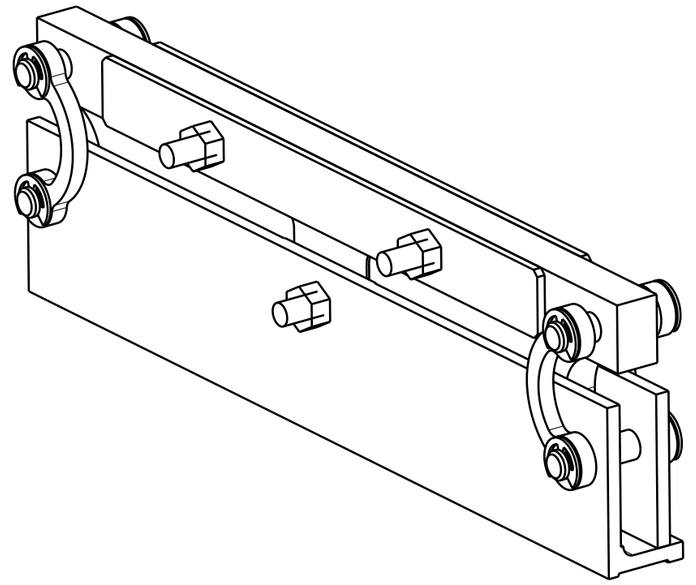

Schnittansicht A-A
Maßstab 2:1

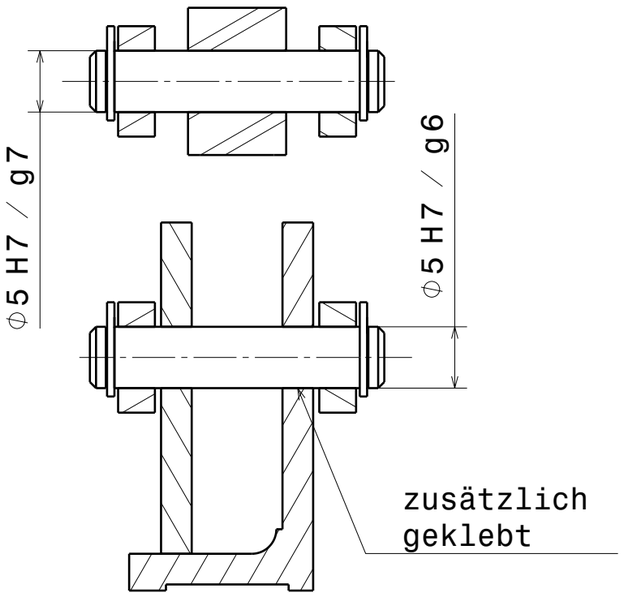

Schnittansicht B-B
Maßsatb 2:1

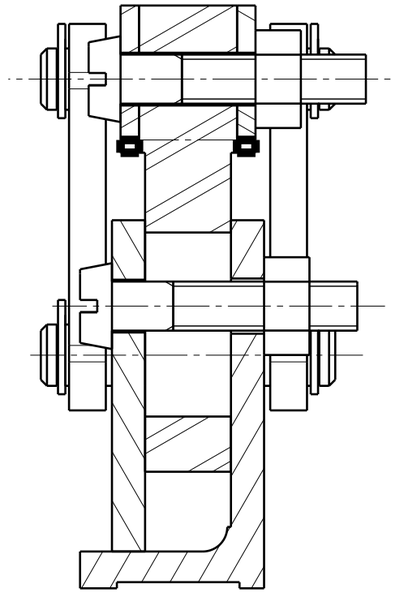

1	2	3	4	5	6
Pos.	Menge	Einheit	Benennung	Sachnummer/Norm-Kurzbezeichnung	Bemerkung
		Stück			

Kanten ISO 13715 -0,2 +0,2	Allgemeintoleranz ISO 2768 - fK
	Oberflächen EN ISO 1302

DLR **Deutsches Zentrum für Luft- und Raumfahrt** e.V.
in der Helmholtz-Gemeinschaft
Institut für Fahrzeugkonzepte

Bei Übermittlung schutzfähiger Informationen behält sich das DLR e.V. alle Rechte für den Fall der Patenterteilung vor.
Jede Verfügungsbefugnis, wie Kopier- und Weitergaberecht, liegt bei uns.

Werkstoff	Gewicht	CAD-Sys.
		CatiaV5 R19

Verantwortl.Abt.	Tech. Referenz	Erstellt durch	Genehmigt von	Maßstab
AEW-IAS	Lars Weyh	Martin Daskalov	.	1:1 (2:1)

Tel.	Dokumentenart	Dokumentenstatus
0711/6862-557	Baugruppenzeichnung	freigegeben

Titel

Tuned Mass Damper

IAS-204-xx-xx-xxx

Änd.	Ausgabedatum	Format	Blatt
0	2016-mm-tt	A3	1/1

Änd. Ziffer	Feld	Datum	Geaendert	Genehmigt	Beschreibung der Aenderung und Aenderungsterminschluessel

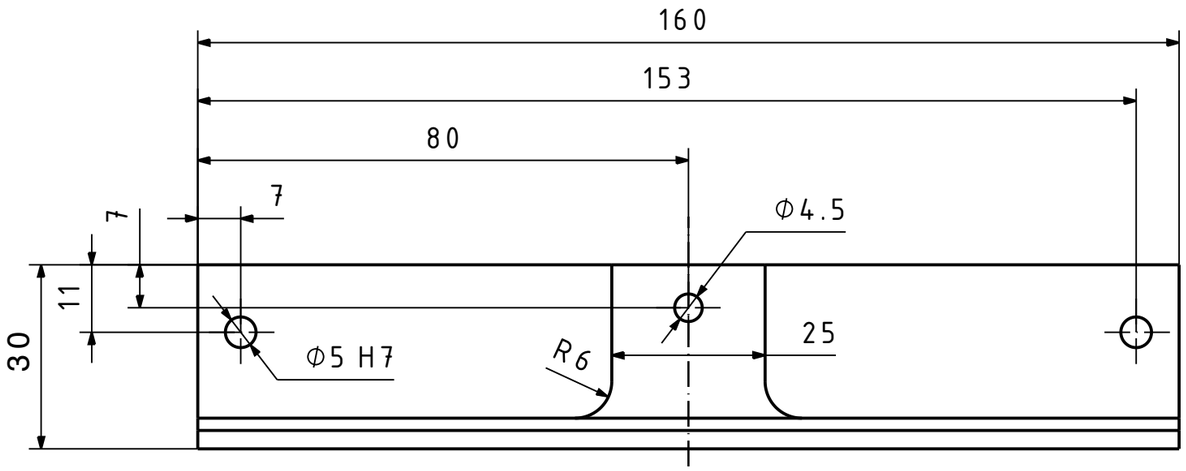

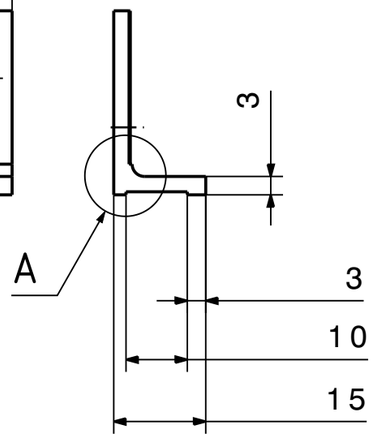

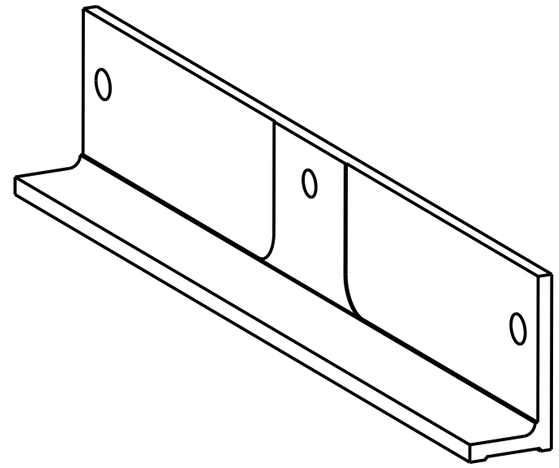

Detail A
Maßstab: 10:1

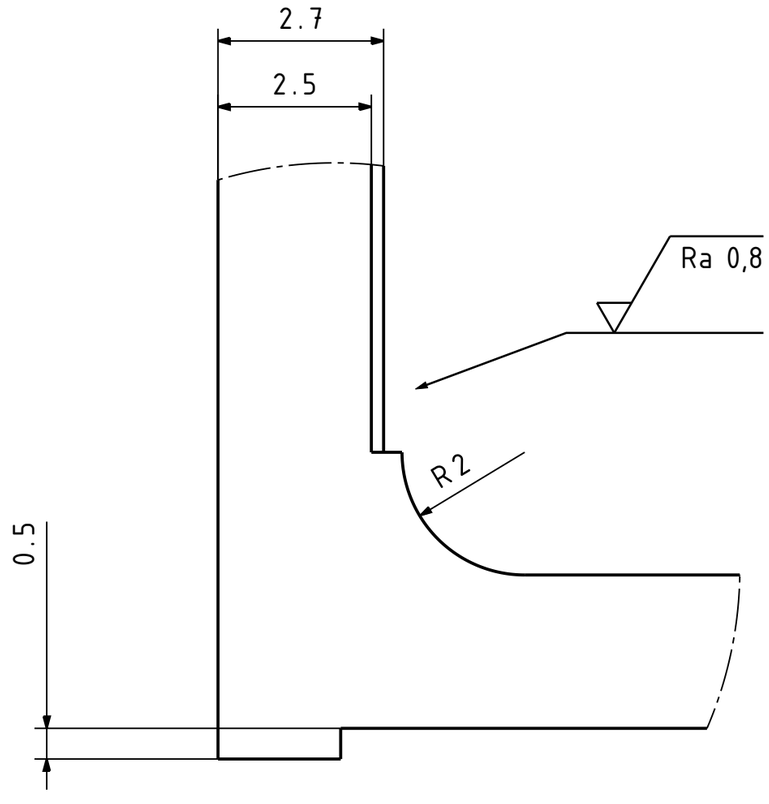

Ra 3,2 (Ra 0,8)

Das Teil ist aus Stahl-L-Profil 30×20×3 herzustellen.

Kanten ISO 13715 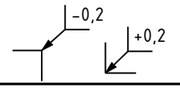	Allgemeintoleranz ISO 2768 - fK	
	Oberflächen EN ISO 1302	

Deutsches Zentrum für Luft- und Raumfahrt e.V.
in der Helmholtz-Gemeinschaft
Institut für Fahrzeugkonzepte

Bei Übermittlung schutzfähiger Informationen behält sich das DLR e.V. alle Rechte für den Fall der Patenterteilung vor.
Jede Verfügungsbefugnis, wie Kopier- und Weitergaberecht, liegt bei uns.

Werkstoff	Gewicht	CAD-Sys.
1.0038 (S235JR, L-Profil)	0,15 kg	Catia V5

Verantwortl.Abt.	Tech. Referenz	Erstellt durch	Genehmigt von	Maßstab
AEW-IAS	Lars Weyh	Martin Daskalov	.	1:1 (10:1)

Tel.	Dokumentenart	Dokumentenstatus
0711/6862-8135	Fertigungszeichnung	freigegeben

Titel				
Base	IAS-204-xx-01-005			
	Änd.	Ausgabedatum	Format	Blatt
	0	2026-02-05	A3	1/1

Änd. Ziffer	Feld	Datum	Geaendert	Genehmigt	Beschreibung der Aenderung und Aenderungsterminschluessel

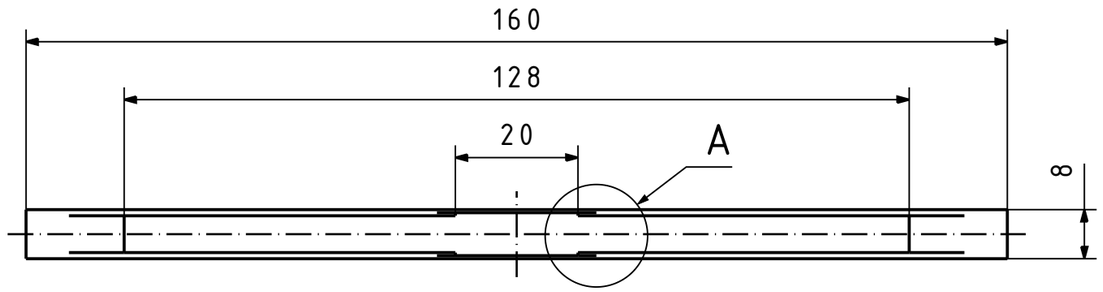

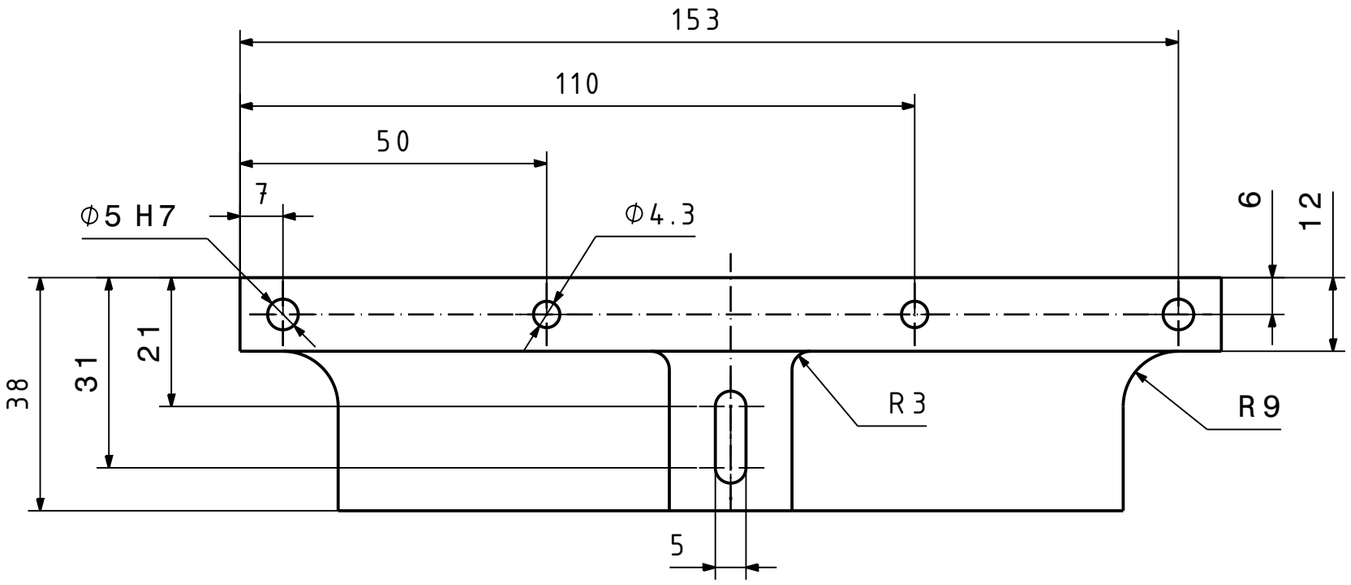

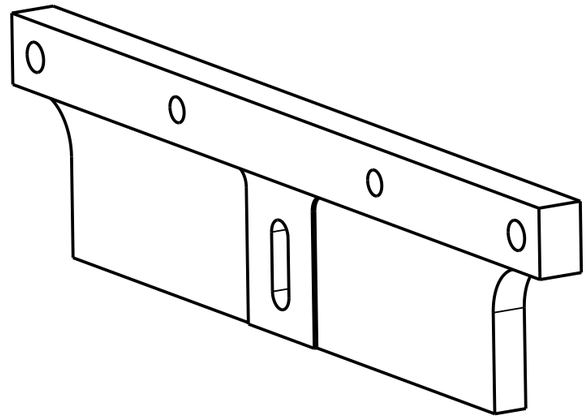

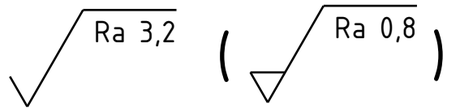

Detail A
Maßstab: 5:1

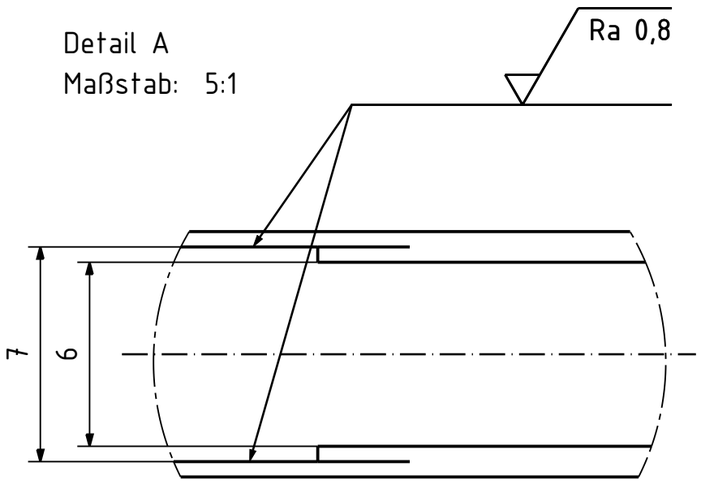

Kanten ISO 13715 −0,2 +0,2	Allgemeintoleranz ISO 2768 - fK		
	Oberflächen EN ISO 1302		
DLR **Deutsches Zentrum für Luft- und Raumfahrt** e.V. in der Helmholtz-Gemeinschaft Institut für Fahrzeugkonzepte	Bei Übermittlung schutzfähiger Informationen behält sich das DLR e.V. alle Rechte für den Fall der Patenterteilung vor. Jede Verfügungsbefugnis, wie Kopier- und Weitergaberecht, liegt bei uns.		
Werkstoff: 3.3206 (AW-6060-T6)	Gewicht: 0,104 kg	CAD-Sys.: Catia V5	
Verantwortl.Abt.: AEW-IAS	Tech. Referenz: Lars Weyh	Erstellt durch: Martin Daskalov	Genehmigt von: .	Maßstab: 1:1 (5:1)
Tel.: 0711/6862-8135	Dokumentenart: Fertigungszeichnung	Dokumentenstatus: freigegeben	
Titel: Middle Plate	IAS-xxx-xx-01-002		
	Änd.: 0	Ausgabedatum: 2026-02-10	Format: A3	Blatt: 1/1

Änd. Ziffer	Feld	Datum	Geaendert	Genehmigt	Beschreibung der Aenderung und Aenderungsterminschluessel

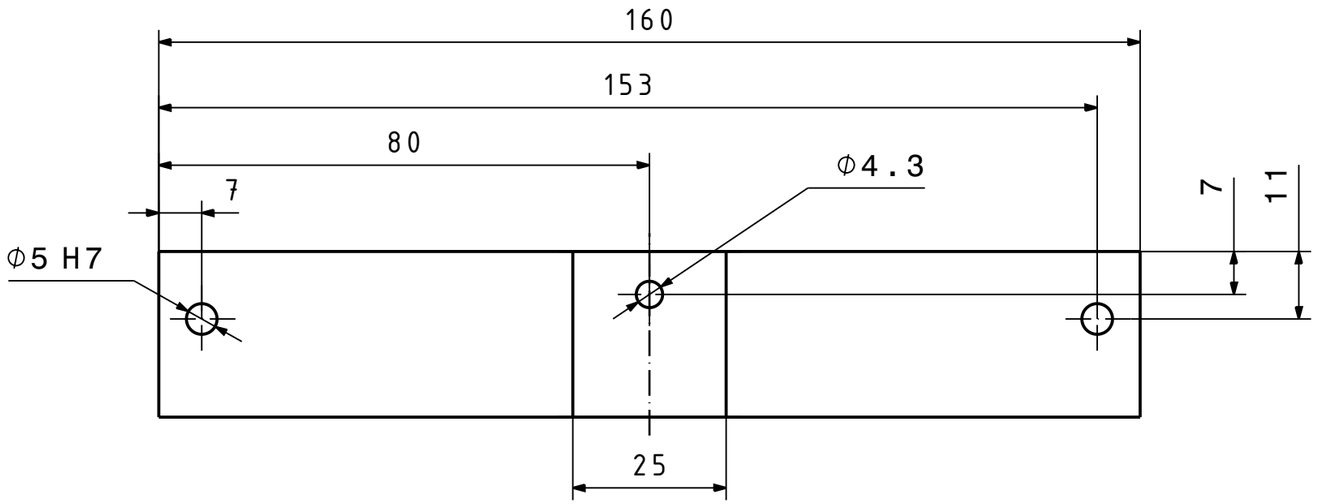

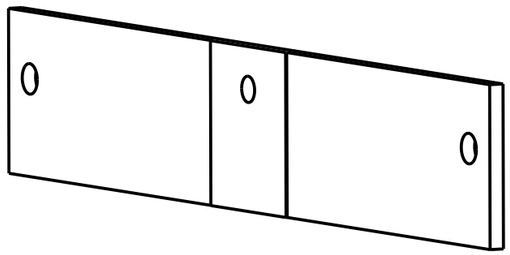

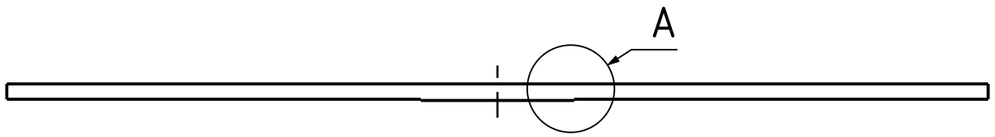

Detail A
Maßstab: 5:1

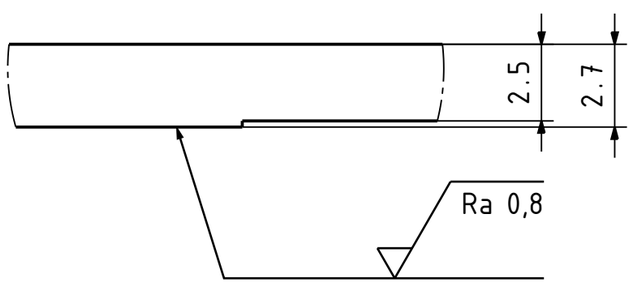

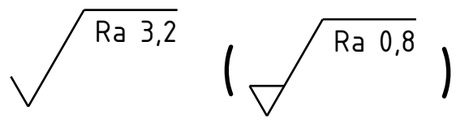

Kanten ISO 13715 $^{+0,2}_{-0,2}$

Allgemeintoleranz ISO 2768 - fK

Oberflächen EN ISO 1302

Deutsches Zentrum für Luft- und Raumfahrt e.V.
in der Helmholtz-Gemeinschaft
Institut für Fahrzeugkonzepte

Bei Übermittlung schutzfähiger Informationen behält sich das DLR e.V. alle Rechte für den Fall der Patenterteilung vor.
Jede Verfügungsbefugnis, wie Kopier- und Weitergaberecht, liegt bei uns.

Werkstoff	Gewicht	CAD-Sys.
1.0038 (S235JR)	0,1 kg	Catia V5

Verantwortl.Abt.	Tech. Referenz	Erstellt durch	Genehmigt von	Maßstab
AEW-IAS	Lars Weyh	Martin Daskalov	.	1:1 (5:1)

Tel.	Dokumentenart	Dokumentenstatus
0711/6862-8135	Fertigungszeichnung	freigegeben

Titel

Outer plate

IAS-204-xx-01-001

Änd.	Ausgabedatum	Format	Blatt
0	2026-05-10	A3	1/1

Änd. Ziffer	Feld	Datum	Geaendert	Genehmigt	Beschreibung der Aenderung und Aenderungsterminschluessel

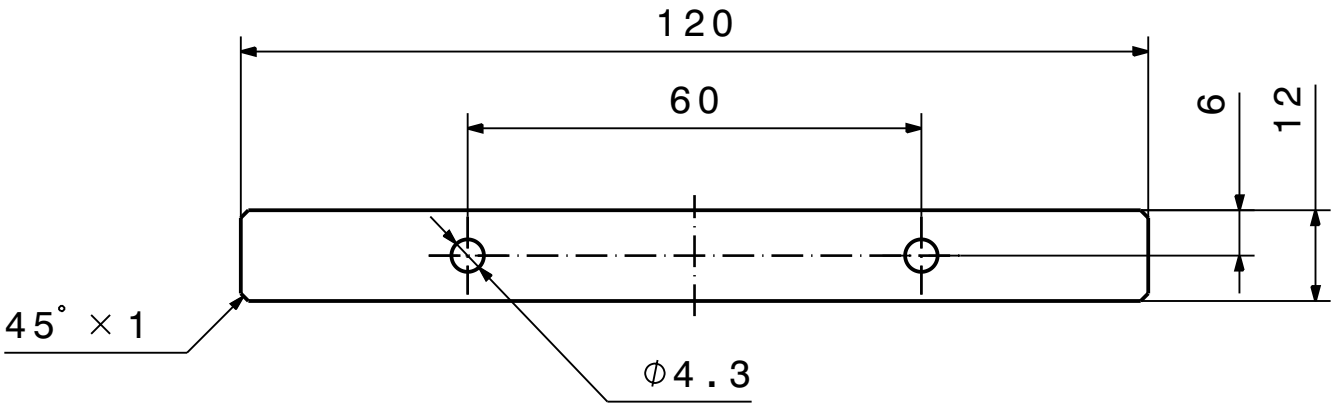

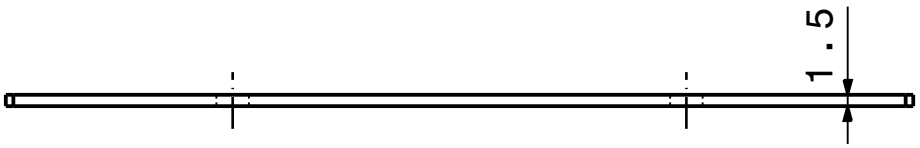

Kanten ISO 13715 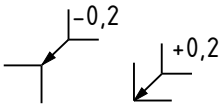

Allgemeintoleranz ISO 2768 - fK

Oberflächen EN ISO 1302

Deutsches Zentrum für Luft- und Raumfahrt e.V.
in der Helmholtz-Gemeinschaft
Institut für Fahrzeugkonzepte

Bei Übermittlung schutzfähiger Informationen behält sich das DLR e.V. alle Rechte für den Fall der Patenterteilung vor.
Jede Verfügungsbefugnis, wie Kopier- und Weitergaberecht, liegt bei uns.

Werkstoff	Gewicht	CAD-Sys.
3.3206 (AW-6060-T6)	0,006 kg	Catia V5

Verantwortl.Abt.	Tech. Referenz	Erstellt durch	Genehmigt von	Maßstab
AEW-IAS	Lars Weyh	Martin Daskalov	-	1:1

Tel.	Dokumentenart	Dokumentenstatus
0711/6862-8135	Fertigungszeichnung	freigegeben

Titel

Weight plate

IAS-xxx-xx-01-004

Änd.	Ausgabedatum	Format	Blatt
0	2026-02-10	A4	1/1

Änd. Ziffer	Feld	Datum	Geaendert	Genehmigt	Beschreibung der Aenderung und Aenderungsterminschluessel

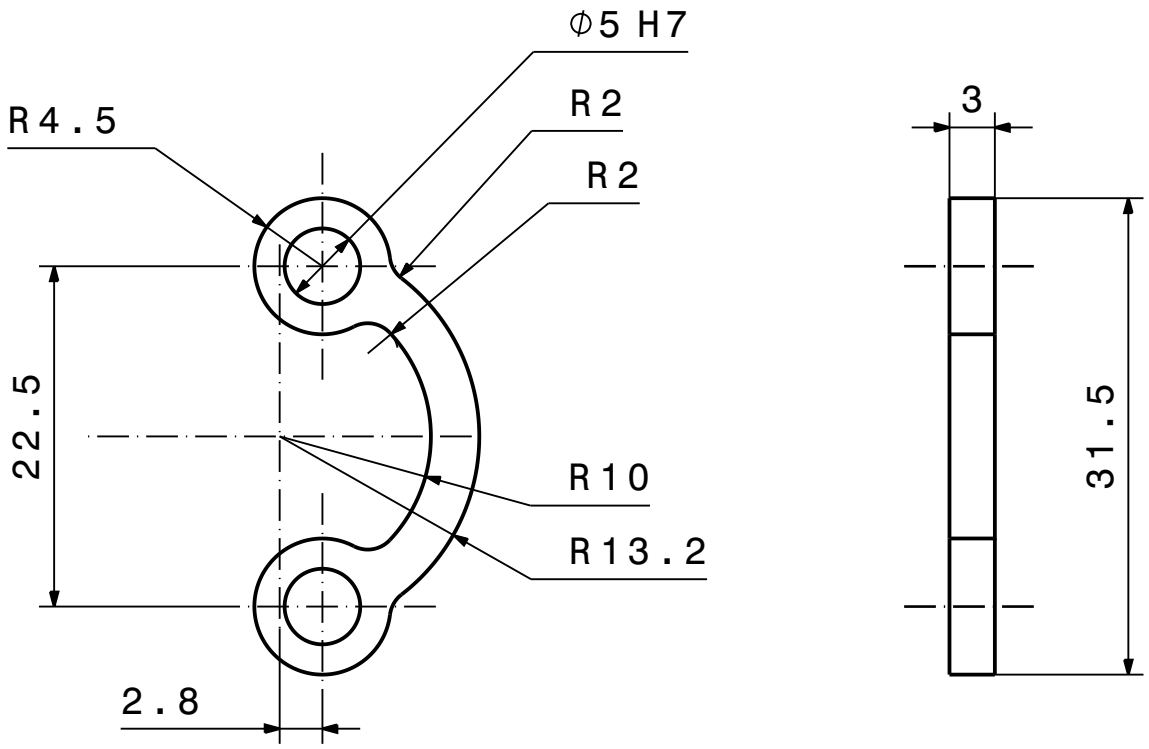

Kanten ISO 13715 $^{-0,2}_{+0,2}$

Allgemeintoleranz ISO 2768 - fK

Oberflächen EN ISO 1302

DLR **Deutsches Zentrum für Luft- und Raumfahrt** e.V.
in der Helmholtz-Gemeinschaft
Institut für Fahrzeugkonzepte

Bei Übermittlung schutzfähiger Informationen behält sich das DLR e.V. alle Rechte für den Fall der Patenterteilung vor.
Jede Verfügungsbefugnis, wie Kopier- und Weitergaberecht, liegt bei uns.

Werkstoff	Gewicht	CAD-Sys.
1.0503 (C45)	0,007 kg	Catia V5

Verantwortl.Abt.	Tech. Referenz	Erstellt durch	Genehmigt von	Maßstab
AEW-IAS	Lars Weyh	Martin Daskalov	-	2:1

Tel.	Dokumentenart	Dokumentenstatus
0711/6862-8135	Fertigungszeichnung	freigegeben

Titel

Leaf spring

IAS-204-xx-01-003

Änd.	Ausgabedatum	Format	Blatt
0	2026-02-10	A4	1/1

G Tools

Claude by Anthropic was used for grammar and spelling correction of the self written Chapters 2, 4, 5, 6. For Chapters 1,3,7 and 8, Claude was used to generate an initial draft which was subsequently edited and revised by the author.

List of Frequently Used Symbols

Latin Notation

A_C	Nominal contact area
B_r	Radial component of air gap flux density
B_t	Tangential component of air gap flux density
d	Damper element
E	Young's modulus
E^*	Composite elastic modulus
E_r	Reuss elastic modulus
E_v	Voigt elastic modulus
F	Friction force
f_{exc}	Excitation frequency
f_i	Slip force
F_N	Normal force
G	Shear modulus
G^*	Composite shear modulus
H	Number of retained harmonics
k	Spring stiffness
k_T	Tangential contact stiffness
$k_{t,\text{rough}}$	Tangential contact stiffness, rough surface contribution
$k_{t,\text{smooth}}$	Tangential contact stiffness, smooth surface contribution
k_x	Jenkins element spring stiffness
m	Absorber mass
m_0	Primary structure mass
n	Number of Jenkins elements in positive yield state
N	Total number of Jenkins elements
n_{rpm}	Rotational speed
p	Nominal contact pressure
p_r	Radial Maxwell stress (force per unit area)
$P_{\mu\nu}$	Amplitude of spatial-temporal force harmonic
$q(t)$	Displacement response
Q_0	Constant Fourier coefficient of displacement
$Q_{c,k}$	Cosine Fourier coefficient of displacement, harmonic k
$Q_{s,k}$	Sine Fourier coefficient of displacement, harmonic k

Ra	Arithmetic mean surface roughness

Greek Notation

α	Rayleigh mass damping coefficient
β	Rayleigh stiffness damping coefficient
ϑ	Circumferential position
μ	Spatial harmonic order
μ_0	Air gap permeability
μ_s	Static friction coefficient
ν	Temporal harmonic order; Poisson's ratio
$\hat{\nu}$	Peak velocity amplitude
$\varphi_{\mu\nu}$	Phase angle of spatial-temporal harmonic
φ_1, φ_2	Volume fractions of constituent materials
ω	Angular frequency
ω_r	Fundamental electrical angular frequency
ζ_i	Modal damping ratio at mode i

Vectors and Matrices

$\boldsymbol{A}$	System matrix
$\boldsymbol{a}$	Column vector
$\boldsymbol{a}^{\mathrm{T}}$	Row vector (transposed column vector)
$\boldsymbol{D}$	Damping matrix
$\boldsymbol{D}^{\mathrm{red}}$	Reduced damping matrix
$\hat{\boldsymbol{f}}$	Physical force vector
$\hat{\boldsymbol{f}}'$	Projected force vector in reduced basis
$\boldsymbol{K}$	Stiffness matrix
$\boldsymbol{K}^{\mathrm{red}}$	Reduced stiffness matrix
$\boldsymbol{M}$	Mass matrix
$\boldsymbol{M}^{\mathrm{red}}$	Reduced mass matrix
$\boldsymbol{T}$	Rubin transformation matrix
$\boldsymbol{U}^{\mathrm{K}}$	Free interface normal modes
$\boldsymbol{\Psi}$	Static constraint modes

Indices and other symbols

$\hat{(\,)}$	Complex quantity
$(\,)^{\mathrm{T}}$	Transposed matrix
$(\,)^{-1}$	Inverse matrix
$(\,)^{\mathrm{red}}$	Quantity in reduced basis

$(\,)^{\mathrm{opt}}$	Optimal value
$(\,)_{1,2}$	Material constituent 1 or 2
$\mathrm{Re}\{\,\}$	Real part
$\mathrm{Im}\{\,\}$	Imaginary part

Bibliography

[1] Acroni, SIJ: M270-35A. 2023. – Forschungsbericht

[2] Ahmadian, M. ; Jeric, K. M.: On the application of shunted piezoceramics for increasing acoustic transmission loss in structures. In: *Journal of Sound and Vibration* 243 (2001), 5, S. 347–359. – ISSN 0022460X

[3] Andonovski, Nemanja ; Moglie, Franco ; Lenci, Stefano ; Sen, Mihir ; Sun, B. ; Wu, Z. Q. ; Jauregui-Correa, J. C. ; Rade, D. A. ; Castello, D. A. ; Jauregui, Juan C. (Hrsg.): *Nonlinear Structural Dynamics and Damping*. ISSN, 11 2018

[4] Anthropic: *Dynamic Vibration Absorber Thesis – Motivation, Abstract and Conclusions*. Generative AI Model, 2026

[5] Argandona, Eneko S. ; Zabala, Alaitz ; Galdos, Lander ; Mendiguren, Joseba: The effect of material surface roughness in aluminum forming. In: *Procedia Manufacturing* Bd. 47, Elsevier B.V., 2020. – ISSN 23519789, S. 591–595

[6] Bao, Xiaoqi ; Varadan, V V. ; Varadan, V K.: Active control of sound transmission through a plate using a piezoelectric actuator and sensor. In: *Smart Materials and Structures* 4 (1995), 12, S. 231–239. – ISSN 0964–1726

[7] Barbieri, Nilson ; Barbieri, Renato: Dynamic analysis of stockbridge damper. In: *Advances in Acoustics and Vibration* (2012). – ISSN 16876261

[8] Bowden, Frank P. ; Tabor, David.: *The friction and lubrication of solids*. Clarendon Press ; Oxford University Press, 1954. – 374 S. – ISBN 9780198507772

[9] Chai, Feng ; Li, Yi ; Pei, Yulong ; Li, Zongyang: Accurate modelling and modal analysis of stator system in permanent magnet synchronous motor with concentrated winding for vibration prediction. In: *IET Electric Power Applications* 12 (2018), 9, S. 1225–1232. – ISSN 17518679

[10] Choi, Young ; Wereley, Norman M.: Vibration Isolation Performance of an Adaptive Magnetorheological Elastomer-Based Dynamic Vibration Absorber. In: *Actuators* 11 (2022), 6. – ISSN 20760825

[11] Cook, Robert D. ; Malkus, David S. ; Plesha, Michael E. ; Witt, Robert J. ; Cook, Robert D.: *Concepts and applications of finite element analysis*. John Wiley & Sons, 2002. – 719 S. – ISBN 0471356050

[12] Dasgupta, Shambhu P. ; Sharjah, U A E.: Computation of Rayleigh Damping Coefficients for Large Systems. 2003. – Forschungsbericht

[13] Deng, Wenzhe ; Zuo, Shuguang: Electromagnetic vibration and noise of the permanent-magnet synchronous motors for electric vehicles: An overview. In: *IEEE Transactions on Transportation Electrification* Bd. 5, Institute of Electrical and Electronics Engineers Inc., 3 2019. – ISSN 23327782, S. 59–70

[14] Doncker, Rik D. ; Sauer, Dirk: Skript zur Tagung - Elektrische Antriebe - Vibrationen und Geräusche. (2024), 2

[15] Ede, Jason D. ; Zhu, Z. Q. ; Howe, David: Rotor resonances of high-speed permanent-magnet brushless machines. In: *IEEE Transactions on Industry Applications* 38 (2002), 11, S. 1542–1548. – ISSN 00939994

[16] Elahinia, Mohammad ; Ciocanel, Constantin ; Nguyen, The M. ; Wang, Shuo: MR- and ER-Based Semiactive Engine Mounts: A Review. In: *Smart Materials Research* 2013 (2013), 2, S. 1–21. – ISSN 2090–3561

[17] FitzGerald, T. F. ; Anagnos, Thalia ; Goodson, Mary ; Zsutty, Theodore: 5. Slotted Bolted Connections in Aseismic Design for Concentrically Braced Connections. In: *Earthquake Spectra* 5 (1989), 5, S. 383–391. – ISSN 8755–2930

[18] Funasaka, Naho ; Isobe, Makoto ; Kosaka, Takashi: Multi-mode Vibration Suppression for Electric Machines using Passive Dynamic Vibration Absorbers Mounting on Stator Outer Peripheral. In: *2024 27th International Conference on Electrical Machines and Systems (ICEMS)*, IEEE, 11 2024. – ISBN 978–4–88686–440–6, S. 2681–2686

[19] García-Tárrago, María J. ; Calaf-Chica, José ; Gómez-Gil, Francisco J.: High-frequency mechanical impedance of rubber mounts: Experimental characterization and resonance mechanisms. In: *European Journal of Mechanics, A/Solids* 113 (2025), 9. – ISSN 09977538

[20] Gieras, Jacek F. ; Wang, Chong ; Lai, Joseph C.: *Noise of Polyphase Electric Motors*. CRC Press, 10 2018. – ISBN 9781420027730

[21] Golub, H. G. ; Loan, Charles F. V.: *Matrix Computations*. 3. 1996. – ISBN 0–8018–5413–8

[22] Gonzalez, Patxi ; Buigues, Garikoitz ; Mazon, Angel J.: *Noise in Electric Motors: A Comprehensive Review*, 7 2023

[23] Greenwood, J A. ; Williamson, ; J B P.: Contact of Nominally Flat Surfaces. 1966. – Forschungsbericht. – 300–319 S

[24] He, Guhuan ; Huang, Zhenyu ; Qin, Ray ; Chen, Dayue: Numerical prediction of electromagnetic vibration and noise of permanent-magnet direct current commutator motors with rotor eccentricities and glue effects. In: *IEEE Transactions on Magnetics* 48 (2012), 5, S. 1924–1931. – ISSN 00189464

[25] Henkel: Hysol 9497. 2014. – Forschungsbericht

[26] Igusa, T. ; Xu, K.: Vibration Control Using Multiple Tuned Mass Dampers. In: *Journal of Sound and Vibration* 175 (1994), 8, S. 491–503. – ISSN 0022460X

[27] Islam, Rakib ; Husain, Iqbal: Analytical model for predicting noise and vibration in permanent-magnet synchronous motors. In: *IEEE Transactions on Industry Applications* 46 (2010), 11, S. 2346–2354. – ISSN 00939994

[28] Jaisee, Sujit ; Yue, Feng ; Ooi, Yi H.: *A state-of-the-art review on passive friction dampers and their applications*, 5 2021

[29] Jenkins, G M.: Analysis of the stress-strain relationships in reactor grade graphite. In: *British Journal of Applied Physics* 13 (1962), 1, S. 30–32. – ISSN 0508–3443

[30] Jin, Haonan ; Gao, Xiangyu ; Ren, Kaile ; Liu, Jinfeng ; Qiao, Liao ; Liu, Mingzi ; Chen, Wei ; He, Yuhang ; Dong, Shuxiang ; Xu, Zhuo ; Li, Fei: *Review on Piezoelectric Actuators Based on High-Performance Piezoelectric Materials*, 11 2022

[31] Johnson, K. L.: *Contact Mechanics*. Cambridge University Press, 5 1985. – ISBN 9780521255769

[32] Kallio, Pasi ; Koivo, H N. ; Lind, Mikael ; Koivo, Heikki N.: Linear motion miniature actuators. 1998. – Forschungsbericht

[33] Kang, Le ; Xia, Jiakuan ; Su, Han ; Li, Zexing ; Liu, Siqi: Online Control Strategy for Radial Vibration Suppression of PMSM by Multiharmonic Current Injection Method. In: *IEEE Transactions on Industrial Electronics* 69 (2022), 9, S. 8692–8704. – ISSN 15579948

[34] Kim, Hae J. ; Jeong, Jae S. ; Yoon, Myung H. ; Moon, Jae W. ; Hong, Jung P.: Simple Size Determination of Permanent-Magnet Synchronous Machines. In: *IEEE Transactions on Industrial Electronics* 64 (2017), 10, S. 7972–7983. – ISSN 02780046

[35] Krack, Malte: Strukturdynamik Skript zur Vorlesung / University of Stuttgart. 2023. – Forschungsbericht

[36] Krack, Malte ; Gross, Johann: *Harmonic Balance for Nonlinear Vibration Problems*. Springer International Publishing, 2019. – ISBN 978–3–030–14022–9

[37] Kraker, A. de ; Campen, D.H. van: Rubin's CMS reduction method for general state-space models. In: *Computers & Structures* 58 (1996), 2, S. 597–606. – ISSN 00457949

[38] Kupferinstitut, Deutsches: Cu-ETP. 2005. – Forschungsbericht

[39] Li, Hui B. ; Zhang, Da ; Xu, Pei Y. ; Cao, Cheng ; Hu, Dong M. ; Yan, Xiao J. ; Song, Zhihuan ; Hu, Zhihong: Analysis on the vibration modes of the electric vehicle motor stator. In: *Vibroengineering Procedia* Bd. 22, EXTRICA, 3 2019. – ISSN 23450533, S. 81–86

[40] Liao, G. J. ; Gong, X. L. ; Kang, C. J. ; Xuan, S. H.: The design of an active-adaptive tuned vibration absorber based on magnetorheological elastomer and its vibration at-

tenuation performance. In: *Smart Materials and Structures* 20 (2011), 7. – ISSN 09641726

[41] Lin, Fu ; Zuo, Shuguang ; Deng, Wenzhe ; Wu, Shuanglong: Modeling and Analysis of Electromagnetic Force, Vibration, and Noise in Permanent-Magnet Synchronous Motor Considering Current Harmonics. In: *IEEE Transactions on Industrial Electronics* 63 (2016), 12, S. 7455–7466. – ISSN 02780046

[42] Lukkunaprasit, Panitan ; Wanitkorkul, Assawin ; Filiatrault, Andre: Performance deterioration of slotted-bolted connection due to bolt impact and remedy by restrainers. In: *13 th World Conference on Earthquake Engineering*, 2004

[43] Marco, Federico D. ; D'amico, Roberto ; Ronzio, Francesca: Electric motor encapsulation design for improved NVH: a CAE-based approach. 2019. – Forschungsbericht

[44] Markiewicz, M: Optimum Dynamic Characteristics of Stockbridge Dampers for Dead-End Spans. 1995. – Forschungsbericht. – 243–256 S

[45] Medina, S. ; Nowell, D. ; Dini, D.: Analytical and numerical models for tangential stiffness of rough elastic contacts. In: *Tribology Letters* 49 (2013), 1, S. 103–115. – ISSN 10238883

[46] Menq, C.-H ; Bielak, J ; Griffin, J H.: The Influence of Microslip on Vibratory Response, Part I: A New Microslip Model. In: *Journal of Sound and Vibration* 107 (1986), S. 279–293

[47] Mokrani, Bilal ; Bastaits, Renaud ; Horodinca, Mihaita ; Romanescu, Iulian ; Burda, Ioanica ; Viguié, Régis ; Preumont, André: Parallel piezoelectric shunt damping of rotationally periodic structures. In: *Advances in Materials Science and Engineering* 2015 (2015). – ISSN 16878442

[48] Ojeda, Xavier ; Mininger, Xavier ; Ahmed, Hamid B. ; Gabsi, Mohamed ; Lécrivain, Michel: Piezoelectric actuator design and placement for switched reluctance motors active damping. In: *IEEE Transactions on Energy Conversion* 24 (2009), S. 305–313. – ISSN 08858969

[49] Park, Chul H. ; Park, Hyun C.: Multiple-Mode Structural Vibration Control Using Negative Capacitive Shunt Damping. 2003. – Forschungsbericht. – 1650–1658 S

[50] Pastor, Miroslav ; Binda, Michal ; Harčarik, Tomáš: Modal assurance criterion. In: *Procedia Engineering* Bd. 48, Elsevier Ltd, 2012. – ISSN 18777058, S. 543–548

[51] Pirnat, Miha ; Čepon, Gregor ; Boltežar, Miha: Introduction of the linear contact model in the dynamic model of laminated structure dynamics: An experimental and numerical identification. In: *Mechanism and Machine Theory* 64 (2013), S. 144–154. – ISSN 0094114X

[52] Praveen, Vijayraghavan ; Krishnan, R: Noise in Electric Machines: A Review / IEEE TRANSACTIONS ON INDUSTRY APPLICATIONS. 1999. – Forschungsbericht

[53] Remus, Niccolò ; Toulabi, Mohammad S. ; Mukundan, Shruthi ; Dhulipati, Himavarsha ; Li, Wenlong ; Novak, Colin ; Kar, Narayan C.: *Electromagnetic Noise and Vibration in PMSM and Their Sources: An Overview*. IEEE, 2020. – ISBN 9781728154428

[54] Saarstahl: C45. 2024. – Forschungsbericht

[55] Sahu, Ashish K. ; Emadi, Ali ; Bilgin, Berker: *Noise and Vibration in Switched Reluctance Motors: A Review on Structural Materials, Vibration Dampers, Acoustic Impedance, and Noise Masking Methods*, 2023

[56] Sahu, Ashish K. ; Selliah, Abeka ; Hassan, Alaa ; Masoumi, Moien ; Bilgin, Berker: Experimental Evaluation of Acoustical Materials for Noise Reduction in an Induction Motor Drive. In: *Machines* 12 (2024), 8. – ISSN 20751702

[57] Sloetjes, P. J. ; Boer, A. D.: Vibration reduction and power generation with piezoceramic sheets mounted to a flexible shaft. In: *Journal of Intelligent Material Systems and Structures* 19 (2008), 1, S. 25–34. – ISSN 1045389X

[58] Soresini, Federico ; Barri, Dario ; Ballo, Federico ; Gobbi, Massimiliano ; Mastinu, Gianpiero: Noise and Vibration Modeling of Permanent Magnet Synchronous Motors: A Review. In: *IEEE Transactions on Transportation Electrification* 10 (2024), S. 8728–8745. – ISSN 23327782

[59] Soresini, Federico ; Barri, Dario ; Ballo, Federico ; Manzoni, Stefano ; Gobbi, Massimiliano ; Mastinu, Giampiero: Noise, Vibration, and Harshness Countermeasures of Permanent Magnet Synchronous Motor with Viscoelastic Layer Material. In: *SAE International Journal of Vehicle Dynamics, Stability, and NVH* 09 (2025), 6, S. 10–09–04–0031. – ISSN 2380–2162

[60] Thomas, D. L.: Dynamics of rotationally periodic structures. In: *International Journal for Numerical Methods in Engineering* 14 (1979), S. 81–102. – ISSN 10970207

[61] thyssenkrupp: AW-6060 / AlMgSi. 2017. – Forschungsbericht

[62] thyssenkrupp: S235JR + AR. 2017. – Forschungsbericht

[63] Tomlinson, G.A.: A molecular theory of friction. In: *The London, Edinburgh, and Dublin Philosophical Magazine and Journal of Science* 7 (1929), 6, S. 905–939. – ISSN 1941–5982

[64] Torregrossa, Dimitri ; Peyraut, François ; Fahimi, Babak ; Mboua, Jérémie ; Miraoui, Abdellatif: Multiphysics finite-element modeling for vibration and acoustic analysis of permanent magnet synchronous machine. In: *IEEE Transactions on Energy Conversion* 26 (2011), 6, S. 490–500. – ISSN 08858969

[65] Vance, John M.: *Rotordynamics of turbomachinery*. Wiley, 1988. – 388 S. – ISBN 9780471802587

[66] Verma, S P. ; Williams, K ; Singal, R K.: Vibrations of Long and Short Laminated Stators of Electrical Machines Part I. 1989. – Forschungsbericht. – 1–13 S

[67] Wagner, H ; Ramamurti, V ; Sastry, R V R. ; Hartmann, K: Dynamics of Stockbridge Dampers. 1973. – Forschungsbericht. – 207–220 S

[68] Wang, C. ; Lai, J. C.: Vibration analysis of an induction motor. In: *Journal of Sound and Vibration* 224 (1999), 7, S. 733–756. – ISSN 0022460X

[69] Xin, Fu L. ; Bai, Xian X. ; Qian, Li J.: Principle, modeling, and control of a magnetorheological elastomer dynamic vibration absorber for powertrain mount systems of automobiles. In: *Journal of Intelligent Material Systems and Structures* 28 (2017), 9, S. 2239–2254. – ISSN 15308138

[70] Xing, Zezhi ; Wang, Xiuhe ; Zhao, Wenliang: Fast Calculation of Electromagnetic Vibration of Surface-Mounted PMSM Considering Teeth Saturation and Tangential Electromagnetic Force. In: *IEEE Transactions on Industrial Electronics* 71 (2024), 1, S. 316–326. – ISSN 15579948

[71] Xu, Jie ; Zhang, Lijun ; Meng, Deijian ; Su, Hui: Simulation, Verification and Optimization Design of Electromagnetic Vibration and Noise of Permanent Magnet Synchronous Motor for Vehicle. In: *Energies* 15 (2022), 8. – ISSN 19961073

[72] Xu, Jingwen ; Tang, Changliang ; He, Shaodong: Research Status and Dynamic Analysis of Damping and Vibration Reduction Technology of Rotating Machinery Rotor System. In: *IET Conference Proceedings* Bd. 2024, Institution of Engineering and Technology, 2024. – ISSN 27324494, S. 161–173

[73] Yan, Bo ; Wang, Ke ; Hu, Zifan ; Wu, Chuanyu ; Zhang, Xinong: *Shunt Damping Vibration Control Technology: A Review*, 2017

[74] Yang, Fan ; Sedaghati, Ramin ; Esmailzadeh, Ebrahim: Vibration suppression of structures using tuned mass damper technology: A state-of-the-art review. In: *JVC/Journal of Vibration and Control* 28 (2022), 4, S. 812–836. – ISSN 17412986

[75] Yu, Shenbo ; Tang, Renyuan: Electromagnetic and mechanical characterizations of noise and vibration in permanent magnet synchronous machines. In: *IEEE Transactions on Magnetics* 42 (2006), S. 1335–1338. – ISSN 00189464

[76] Zhao, G ; Pinte, G ; Devos, S ; Swevers, J ; Sas, P: A piezo-based rotational inertia shaker for the active control of rotating machinery. (2012), 4

[77] Zhou, X. Q. ; Yu, D. Y. ; Shao, X. Y. ; Zhang, S. Q. ; Wang, S.: *Research and applications of viscoelastic vibration damping materials: A review*, 2 2016

[78] Zhu, Z Q. ; Howe, D: Effects of End-Shields and Rotor on Natural Frequencies and Modes of Stator of Small Electrical Machines. In: *1989 Fourth International Conference on Electrical Machines and Drives*, IET, 9 1989. – ISSN 0537–9989